



# A splicing isoform of GPR56 mediates microglial synaptic refinement via phosphatidylserine binding

Tao Li<sup>1,2</sup> , Brian Chiou<sup>1</sup>, Casey K Gilman<sup>2</sup>, Rong Luo<sup>2</sup>, Tatsuhiko Koshi<sup>2</sup>, Diankun Yu<sup>1</sup>, Hayeon C Oak<sup>1</sup>, Stefanie Giera<sup>2</sup>, Erin Johnson-Venkatesh<sup>3</sup>, Allie K Muthukumar<sup>3</sup>, Beth Stevens<sup>3,4</sup>, Hisashi Umemori<sup>3</sup> & Xianhua Piao<sup>1,2,3,5,6,7,\*</sup> 

## Abstract

Developmental synaptic remodeling is important for the formation of precise neural circuitry, and its disruption has been linked to neurodevelopmental disorders such as autism and schizophrenia. Microglia prune synapses, but integration of this synapse pruning with overlapping and concurrent neurodevelopmental processes, remains elusive. Adhesion G protein-coupled receptor ADGRG1/GPR56 controls multiple aspects of brain development in a cell type-specific manner: In neural progenitor cells, GPR56 regulates cortical lamination, whereas in oligodendrocyte progenitor cells, GPR56 controls developmental myelination and myelin repair. Here, we show that microglial GPR56 maintains appropriate synaptic numbers in several brain regions in a time- and circuit-dependent fashion. Phosphatidylserine (PS) on presynaptic elements binds GPR56 in a domain-specific manner, and microglia-specific deletion of *Gpr56* leads to increased synapses as a result of reduced microglial engulfment of PS<sup>+</sup> presynaptic inputs. Remarkably, a particular alternatively spliced isoform of GPR56 is selectively required for microglia-mediated synaptic pruning. Our present data provide a ligand- and isoform-specific mechanism underlying microglial GPR56-mediated synapse pruning in the context of complex neurodevelopmental processes.

**Keywords** adhesion GPCR; GPR56; microglia; phosphatidylserine; synaptic pruning

**Subject Category** Neuroscience

**DOI** 10.15252/embj.2019104136 | Received 27 November 2019 | Revised 20 April 2020 | Accepted 22 April 2020 | Published online 25 May 2020

**The EMBO Journal (2020) 39: e104136**

See also: **G Peet et al** (August 2020)

## Introduction

Microglia, tissue-resident macrophages of the central nervous system (CNS), are important for synaptic development, both in promoting synapse formation (Parkhurst *et al*, 2013; Miyamoto *et al*, 2016) and in engulfing redundant synapses (Paolicelli *et al*, 2011; Schafer *et al*, 2012). Immune molecules such as classical complement components and receptors, CX3CL1/CX3CR1, MHC class I, and PirB have been implicated in developmental synaptic refinement (Stevens *et al*, 2007; Paolicelli *et al*, 2011; Schafer *et al*, 2012; Lee *et al*, 2014; Vainchtein *et al*, 2018; Djuricic *et al*, 2019) and in synapse loss in disease models (Hong *et al*, 2016; Sekar *et al*, 2016; Vasek *et al*, 2016; Bialas *et al*, 2017; Sellgren *et al*, 2019). Mammalian neurodevelopment involves a succession of overlapping processes beginning with neurogenesis and neuronal migration, which are concurrent with microglial infiltration and morphogenesis. Subsequently, neurite arborization sets the stage for synaptogenesis, circuit establishment, and refinement, as well as myelination. All of these processes entail cell–cell interactions; discovery of molecules involved in multiple processes in a cell type-specific fashion can inform our understanding about how overlapping and sequential programs of intercellular signaling events are coordinately regulated.

The adhesion G protein-coupled receptor (aGPCR) ADGRG1/GPR56 controls several aspects of brain development in a cell type-specific manner by mediating cell–cell and cell–matrix interactions (Singer *et al*, 2013; Langenhan *et al*, 2016). During embryonic brain development, GPR56 is expressed in neural progenitor cells and migrating neurons, and interacts with its extracellular matrix (ECM) ligand collagen III to regulate cortical lamination (Luo *et al*, 2011; Jeong *et al*, 2012a,b). In later stages of brain development and throughout postnatal life, GPR56 is highly expressed in glial cells, including astrocytes, oligodendrocyte lineage cells, and microglia (Zhang *et al*, 2014; Bennett *et al*, 2016). We recently showed that oligodendrocyte precursor cell (OPC) GPR56 functions together with its microglia-produced ligand, tissue transglutaminase (TG2, gene

1 Eli and Edythe Broad Center of Regeneration Medicine and Stem Cell Research, University of California, San Francisco (UCSF), San Francisco, CA, USA

2 Department of Medicine, Boston Children's Hospital and Harvard Medical School, Boston, MA, USA

3 F. M. Kirby Neurobiology Center, Children's Hospital, Harvard Medical School, Boston, MA, USA

4 Howard Hughes Medical Institute, Boston Children's Hospital, Boston, MA, USA

5 Weill Institute for Neuroscience, University of California, San Francisco (UCSF), San Francisco, CA, USA

6 Division of Neonatology, Department of Pediatrics, University of California, San Francisco (UCSF), San Francisco, CA, USA

7 Newborn Brain Research Institute, University of California, San Francisco (UCSF), San Francisco, CA, USA

\*Corresponding author. Tel: +1 415 502 3460; E-mail: xianhua.piao@ucsf.edu

symbol *Tgm2*), and an ECM component laminin to control developmental myelination and myelin repair (Ackerman *et al*, 2015; Giera *et al*, 2015, 2018). Consistent with these findings, germline homozygous loss-of-function mutations in *GPR56* cause a compound human brain malformation whose phenotype includes aberrant cortical architecture and dysmyelination (Piao *et al*, 2004, 2005). This phenotype is recapitulated in genetic mouse models indicating conserved GPR56 function (Li *et al*, 2008; Giera *et al*, 2015).

Recent studies showed that *Gpr56* is only expressed in yolk sac-derived microglia but not in microglia-like cells engrafted from fetal liver- and bone marrow-derived hematopoietic stem cells, even after long-term adaptation in the CNS *in vivo* (Bennett *et al*, 2018; Cronk *et al*, 2018). Furthermore, *Gpr56* expression is promptly lost in primary cultures of microglia (Bohlen *et al*, 2017; Gosselin *et al*, 2017). Thus, *Gpr56* is one of few genes that defines the microglial lineage and requires both the appropriate ontogeny and environmental cues for its expression. Motivated by the concept that cell type-specific functions of GPR56 might coordinate multiple sequential and overlapping neurodevelopmental processes, we tested the hypothesis that microglial GPR56 mediates synapse refinement during postnatal life. Our study results uncover that an alternatively spliced isoform of GPR56 is required for microglia-mediated synapse refinement via binding to phosphatidylserine (PS).

## Results

### PS flags retinal ganglion cell (RGC) synaptic inputs for removal by microglia

How do microglia discriminate which synapse to eliminate? PS is a phospholipid that largely resides on the inner leaflet of the plasma membrane under normal conditions (McLaughlin & Murray, 2005). PS externalization serves as an “eat-me” signal for clearance of apoptotic and stressed cells as well as outer segment membranes of retinal photoreceptors (Feng *et al*, 2002; Segawa *et al*, 2011; Neher *et al*, 2013; Tufail *et al*, 2017). Here, we hypothesize that PS flags synapses for removal. To test this hypothesis, we employed the mouse retinogeniculate system, a classic model to study developmental synaptic pruning (Shatz & Kirkwood, 1984; Schafer *et al*, 2012). During early postnatal stage, the axons of RGCs extend into the dorsal lateral geniculate nucleus (dLGN) and form excessive synaptic connections with relay neurons. These RGC synaptic inputs undergo pruning by microglia (Schafer *et al*, 2012). We performed sequential dual labeling with an RGC anterograde tracer—fluorescent cholera toxin B (CTB) and a PS marker—PSVue (Koulov *et al*, 2003; Smith *et al*, 2011), a small PS-binding molecule with superior tissue diffusion than pSIVA (an Annexin B12 derivative that binds PS) (Fig EV1). CTB was intravitreally injected into eyes to trace RGC inputs at P5, and PSVue was injected into the board area between the dLGN and hippocampus at P6 (Fig 1A). Six hours after PSVue injection, fresh mouse brains were sectioned and imaged under a confocal microscope (Fig 1B). We observed PSVue colocalizing with some RGC inputs in the dLGN of WT mice (Fig EV1B). In the developing dLGN, microglial engulfment of synaptic elements peaks at P5 and is dramatically decreased at P10 (Schafer *et al*, 2012). To investigate whether there are more PS<sup>+</sup> synapses during the time point of peak synaptic pruning, we performed dual labeling

of PSVue and CTB at P6 and P13. Indeed, we observed that nearly 10% of RGC inputs were PSVue-positive at P6, but only 3% were PSVue-positive at P13 (Fig 1C and D), coinciding with the rise and fall of microglia-mediated synaptic pruning from P5 to P10. To further confirm PS reside with synaptic structures, we performed immunohistochemistry (IHC) on P6 brain for vesicular glutamate transporter 2 (vGlut2), a presynaptic marker specific to RGC inputs in the dLGN (Land *et al*, 2004), and Homer1, a postsynaptic marker. Indeed, we observed colocalization of PSVue with vGlut2<sup>+</sup> presynapses and Homer1<sup>+</sup> postsynapses (Fig 1E and F).

We next investigated whether microglia engulf PS<sup>+</sup> RGC synaptic inputs by combining the RGC anterograde tracing, PS labeling, and microglial engulfment assays. RGC inputs were labeled with Alexa 488-conjugated CTB via intravitreal injection at P5, and PS exposed synapses were labeled by PSVue via intracranial injection at P6. Brains were harvested 24 hours later at P7 for analysis of microglial phagocytosis (Fig 1B). We first tested the hypothesis that microglia engulf PS<sup>+</sup> presynaptic elements rather than free fluorescent dye by performing a negative control experiment using 5-carboxytetramethylrhodamine (5-TAMRA), the fluorophore component of PSVue that does not bind PS (Hanshaw & Smith, 2005). As shown in Fig EV2, we observed very sparse 5-TAMRA signals in microglia compared to PSVue, supporting the validity of our assay. In WT animals, we observed that PSVue colocalized with RGC inputs inside microglia (Fig EV2B). To examine whether RGC inputs were targeted to lysosome in microglia, we did additional staining against CD68, a lysosomal marker for microglia, and detected internalized PS<sup>+</sup> RGC synaptic inputs colocalized with CD68 (Fig 1G). Moreover, vGlut2<sup>+</sup> presynapses were also colocalized with CD68 and PSVue in microglia (Fig 1H). Next, we quantified the percentage of PS<sup>+</sup> RGC inputs. We saw < 10% RGC inputs outside microglia were PS<sup>+</sup> (Fig 1I and J), but ~73% RGC inputs inside microglia were PS<sup>+</sup> (Fig 1K), suggesting microglia favorably engulf PS<sup>+</sup> synaptic inputs, although they do also engulf PS<sup>-</sup> inputs to a lesser degree (Fig 1K). Taken together, these data demonstrated that exposed PS flags RGC presynapses for removal by microglia during the early development of dLGN.

### GPR56 binds to phosphatidylserine

*Gpr56* transcript increases in microglia from embryonic stage and reaches a high level between P3-P6, a period of active microglia-mediated synaptic pruning (Appendix Fig S1; Matcovitch-Natan *et al*, 2016). Considering the facts that *Gpr56* defines true yolk sac-derived microglia (Matscovitch-Natan *et al*, 2016; Bennett *et al*, 2018; Cronk *et al*, 2018) and that BAI1/ADGRB1, another aGPCR family member, recognizes PS (Park *et al*, 2007), we hypothesized that microglial GPR56 regulates developmental synaptic pruning by binding to PS. GPR56 contains an extensive N-terminal fragment (NTF) followed by a classical seven-transmembrane region and a cytoplasmic tail (Fig 2A; Folts *et al*, 2019). Within the long NTF, there are two functional domains, termed pentraxin/laminin/neurexin/sex-hormone-binding-globulin-like (PLL) and GPCR autoproteolysis inducing (GAIN) domains (Araç *et al*, 2012; Salzman *et al*, 2016). We engineered recombinant proteins of human immunoglobulin Fc (hFc)-tagged full-length NTF (NTF-hFc) and GAIN-hFc (Fig 2B).

We investigated whether GPR56 binds PS on cells using flow cytometry analyses of Ba/F3, an IL-3 dependent murine pro-B cell

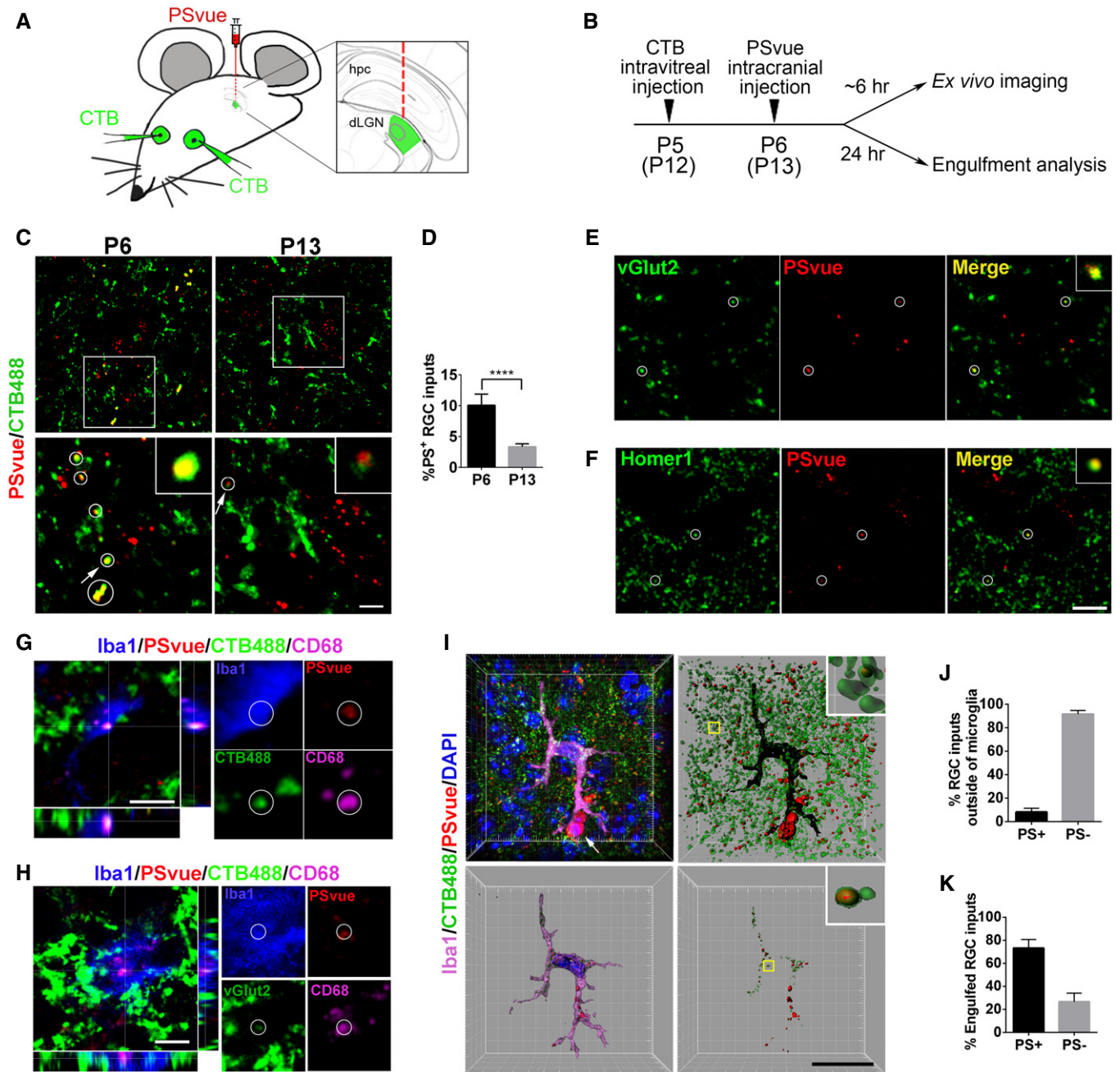


**Figure 1. PS flags RGC inputs for removal by microglia during early dLGN development.**

**A** A schematic drawing of experimental procedure where CTB488 is intraocularly injected, followed by intracranial injection of PSVue550 to dLGN border.

**B** A schematic diagram shows the timeline of procedures for *ex vivo* imaging and engulfment analysis.

**C** Top panel: Representative images show PS labeling in the WT dLGN at P6 and P13. RGC inputs were labeled with CTB488. Bottom panel: Enlarged images of the boxed region in top panels. Circles indicate PS<sup>+</sup> RGC inputs. Arrows point to the enlarged PS<sup>+</sup> RGC inputs in the insets. Scale bar, 5  $\mu$ m.

**D** Quantification of the percentage of PS<sup>+</sup> RGC inputs in total RGC inputs at P6 and P13.  $N = 4$ , \*\*\*\* $P < 0.0001$ . Student's *t*-test.

**E** Co-labeling of vGlut2 and PSVue in the dLGN at P6. Circles indicate colocalized vGlut2 and PSVue.

**F** Co-labeling of Homer1 and PSVue in the dLGN at P6. Circles indicate colocalized Homer1 and PSVue. Scale bar, 5  $\mu$ m.

**G** Orthogonal sections showed a triple-positive PS<sup>+</sup>/CTB488<sup>+</sup>/CD68<sup>+</sup> RGC inputs inside of microglia. Scale bar, 5  $\mu$ m.

**H** Orthogonal sections showed a triple-positive PS<sup>+</sup>/vGlut2<sup>+</sup>/CD68<sup>+</sup> synapse inside of microglia. Scale bar, 5  $\mu$ m.

**I** A representative image of microglia (upper-left) is surface rendered (bottom-left). The white arrow points to cells which might be apoptotic cells labeled by PSVue. RGC inputs and PSVue outside or inside of microglia are shown in the two right panels. Scale bar, 20  $\mu$ m.

**J** Quantification of the percentage of PS<sup>+</sup> and PS<sup>-</sup> RGC inputs outside of microglia in total inputs.  $N = 4$ .

**K** Quantification of the percentage of engulfed PS<sup>+</sup> and PS<sup>-</sup> RGC inputs in total engulfed inputs.  $N = 4$ .

Data information: Data are presented as mean  $\pm$  SD.

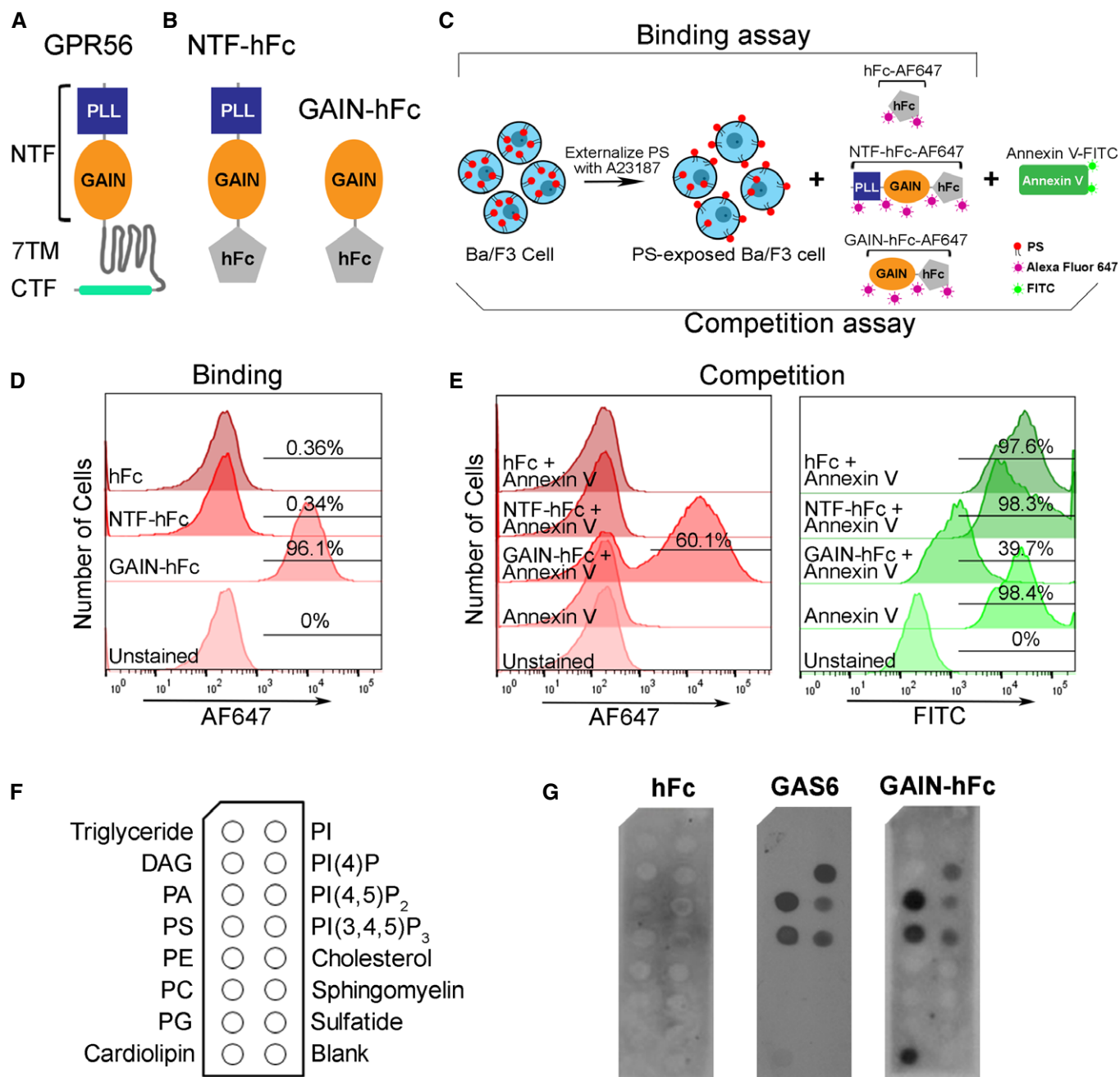


**Figure 2. GPR56 binds to PS.**

**A** A schematic drawing of GPR56 protein structure, with a N-terminal fragment (NTF), a seven-transmembrane domain (7-TM) and a C-terminal fragment (CTF).

**B** A diagram shows the hFc tag was added to the c-terminal of GPR56-NTF (NTF-hFc) or GAIN domain (GAIN-hFc).

**C** A flowchart showing the experimental design of flow cytometry analysis. Briefly, Ba/F3 cells are treated with A23187 to externalize PS. For the binding assay, Alexa Fluor 647-conjugated hFc, GAIN-hFc, or NTF-hFc were incubated with PS-externalized Ba/F3 cells. For the competition assay, Alexa Fluor 647-conjugated hFc, GAIN-hFc, or NTF-hFc were used to compete with FITC-conjugated Annexin V binding.

**D** The binding experiment using flow cytometry show that only the GAIN domain binds to PS, similar as Annexin V binding.

**E** In the competition experiment, AF647 channel shows that GAIN domain binds 60.1% of the PS<sup>+</sup> Ba/F3 cells (left). Correspondingly, FITC channel reveals 39.7% Annexin V binding to PS<sup>+</sup> Ba/F3 cells (right).

**F** A diagram of membrane lipid strips spotted with fifteen different lipids. DAG, diacylglycerol; PA, phosphatidic acid; PE, phosphatidylethanolamine; PC, phosphatidylcholine; PG, phosphatidylglycerol; PI, phosphatidylinositol.

**G** Direct binding of hFc-tagged GPR56 GAIN proteins to PS and other phospholipids. HFc was used as a negative control, and GAS6 as a positive control.

line that externalizes PS upon calcium ionophore A23187 treatment (Appendix Fig S2; Suzuki *et al*, 2010). We first performed a direct binding assay using Alexa Fluor 647 (AF647)-labeled full-length NTF, GAIN domain, or hFc (Fig 2C). FITC-conjugated Annexin V, a known PS-binding protein (Koopman *et al*, 1994), served as a positive control. Unexpectedly, we found that only the GAIN domain, not the full-length NTF, bound PS (Fig 2D). To further verify this observation, we performed a competition assay, in which labeled full-length NTF, GAIN domain, or hFc was used to displace Annexin V binding (Fig 2C). Indeed, we confirmed that the GAIN domain, but not full-length NTF, competed with Annexin V for binding to PS (Fig 2E). The PLL and GAIN domains are constrained by an interdomain disulfide bond at two cysteine residues C121 and C177 (Salzman *et al*, 2016). It is conceivable that the PLL domain blocks GAIN domain binding to PS in the full-length NTF.

To test whether GPR56 GAIN domain binds to other phospholipids besides PS, we performed a protein–lipid overlay experiment using membrane lipid strips, as previously described (Park *et al*, 2007). GAS6, a known PS-binding protein, was used as a positive control. Interestingly, we found GAIN domain has a similar lipid-binding profile as GAS6, except cardiolipin (Fig 2F and G). In this *in vitro* membrane-based assay, GPR56 GAIN domain was able to bind phosphatidic acid (PA), phosphatidylserine (PS), cardiolipin, PI(4)P, PI(4,5)P<sub>2</sub>, and PI(3,4,5)P<sub>3</sub>. Given that PA, PI(4)P, PI(4,5)P<sub>2</sub>, and PI(3,4,5)P<sub>3</sub> are normally present on the inner leaflet of the cell plasma membrane (Ingólfsson *et al*, 2014), and cardiolipin is a phospholipid almost exclusively located in the inner mitochondrial membrane (Paradies *et al*, 2014), GAIN domain binding to those lipids carries unclear biological relevance in the context of our current study.

### **GPR56 S4 variant is dispensable for cortical development and CNS myelination but is essential for microglia-mediated synaptic refinement**

S4 is an alternatively spliced GPR56 isoform that initiates at an alternative ATG start codon in exon 4, resulting in a GPR56 variant that contains only the GAIN domain in its extracellular region, in both humans and mice (Fig 3A; Kim *et al*, 2010; Salzman *et al*, 2016). We published the cortical phenotype of the germline *Gpr56* gene-targeted mice (Li *et al*, 2008), before the discovery of *Gpr56* splicing variants. At that time, our data suggested that this line represented a null allele in regard to cortical phenotype. Subsequently, it was characterized as a hypomorphic allele, represented by selective expression of the *Gpr56 S4* variant (Fig 3B, Appendix Fig S3; Salzman *et al*, 2016). In the present report, this genetic model is referred to as *Gpr56 S4* (Fig 3C). To extend our investigation of *Gpr56* biology, we deleted *Gpr56* exons 4–6, yielding a global null mutant termed as *Gpr56 null*, lacking both full-length GPR56 and its S4 variant (Fig 3C). Based on the fact that the PLL domain binds collagen III (Luo *et al*, 2012), which is the relevant GPR56 ligand in the developing cerebral cortex, we speculated that the S4 isoform would not be required for cerebral cortical lamination. Indeed, we observed a comparable cortical ectopia size and distribution between *Gpr56 S4* and *Gpr56 null* mice (Fig 3D–F). GPR56 also drives myelination and myelin repair via the PLL domain and TG2 interaction (Singer *et al*, 2013; Giera *et al*, 2015, 2018). As we expected, we observed comparable decreased myelination in *Gpr56*

*null* and *Gpr56 S4* mice (Fig 3G and H), which suggested that the GPR56 S4 isoform is dispensable in OPC GPR56 regulation of CNS myelination.

Based on PS-binding data (Fig 2), we hypothesized that GPR56 S4 would be required for microglia-mediated synaptic pruning. Supporting this hypothesis, we found that *Gpr56 S4* is the major transcript in microglia as determined by qPCR analysis of microglia isolated from P5 and P14 wild-type (WT) mouse brains (Fig 3I). To test whether GPR56 S4 is implicated in synaptic refinement, we first examined synaptic density in the dLGN (Schafer *et al*, 2012). To visualize retinogeniculate synaptic connections, we performed double immunohistochemistry (IHC) for vGlut2 and Homer1, followed by confocal imaging in the dLGN core region (Fig 3J), to resolve juxtaposed pre- and postsynaptic structures. Colocalized vGlut2 and Homer1 puncta (vGlut2<sup>+</sup>/Homer1<sup>+</sup>) were counted as retinogeniculate synapses. Strikingly, germline *Gpr56 null* exhibited significantly increased synapse density at P10, while *Gpr56 S4* and controls showed comparable synapse density (Fig 3K and L). Interestingly, we observed significantly increased vGlut2<sup>+</sup> presynaptic signals, but not Homer1<sup>+</sup> postsynaptic inputs (Appendix Fig S4). Taken together, our results support that the GPR56 S4 isoform is crucial to synapse development.

To delineate whether this change resulted from a reduction in microglial engulfment of synapses, we performed *in vivo* engulfment assays as previously described (Schafer *et al*, 2012; Vainchtein *et al*, 2018). Mice received intraocular injection of CTB at P4 and were sacrificed 24 hours later for analysis, as peak pruning occurs around P5 in the murine retinogeniculate system (Fig 3M). Indeed, *Gpr56 null* microglia exhibited significantly reduced engulfment of RGC inputs, while *Gpr56 S4* microglia showed a comparable engulfment ability as controls (Fig 3N and O). Taken together, these results support the concept that the GPR56 S4 isoform is essential to microglia-mediated synaptic pruning.

### **Deleting microglial *Gpr56* results in excess synapses in the dLGN during postnatal development**

To specifically investigate the function of microglial GPR56 in synaptic refinement, we generated microglia-specific *Gpr56* conditional knockout mice by crossing mice harboring a conditional *Gpr56<sup>fl/fl</sup>* allele (Giera *et al*, 2015) with *Cx3cr1-Cre* transgenic mice (Yona *et al*, 2013). Since *Cx3cr1-Cre* is a direct knock-in transgenic mouse line, we used *Gpr56<sup>fl/fl</sup>; Cx3cr1-Cre<sup>+/-</sup>* mice as conditional knockouts (CKO) and *Gpr56<sup>+/-</sup>; Cx3cr1-Cre<sup>+/-</sup>* as controls. Western blot and qPCR experiments did not detect GPR56 protein or *Gpr56* transcript in microglia isolated from CKOs and their controls (Fig EV3A and B). We further performed RNAscope analysis for *Gpr56* in the prefrontal cortex of P30 mice (Fig 4A). We detected minimal, if any, *Gpr56* transcripts in *Gpr56 null* and CKO microglia, comparing to controls (Fig 4B). In contrast, *Gpr56* transcripts were abundant in non-microglial cells in both CKO and controls (Fig 4B), confirming *Gpr56* was cell-specifically deleted in microglia. To further confirm the specificity of Cre-Lox recombination in microglia under the *Cx3cr1-Cre* driver, we crossed *Cx3cr1-Cre* with a reporter line *Rosa-GFP<sup>fl</sup>* and demonstrated restricted GFP expression in microglia (Appendix Fig S5). To investigate whether deleting microglial *Gpr56* affected microglial cellular properties, we asked whether there were differences between control and CKO in microglial cell

density, coverage, morphology, and amounts of phagocytic machinery (defined as %CD68<sup>+</sup> cells) in the dLGN of P5 mice. This comprehensive analysis showed no significant differences (Fig EV3C–J), enabling a functional evaluation of microglial GPR56 in synapse development.

We first conducted a time course study of synaptic density from P0 to P10 in the dLGN. At birth (P0), we observed comparable

retinogeniculate synapse density (vGlut2<sup>+</sup>/Homer1<sup>+</sup>) between CKO mice and their controls. At P5 and P10, we observed a steady increase in synaptic density by ~21% and 35%, respectively, in CKO mice compared to their age- and sex-matched controls (Fig 4C and D, Appendix Fig S6). To further confirm this phenotype, we applied structured illumination microscopy (SIM) to resolve juxtaposed pre- and postsynaptic structures with a higher resolution (Hong *et al*,

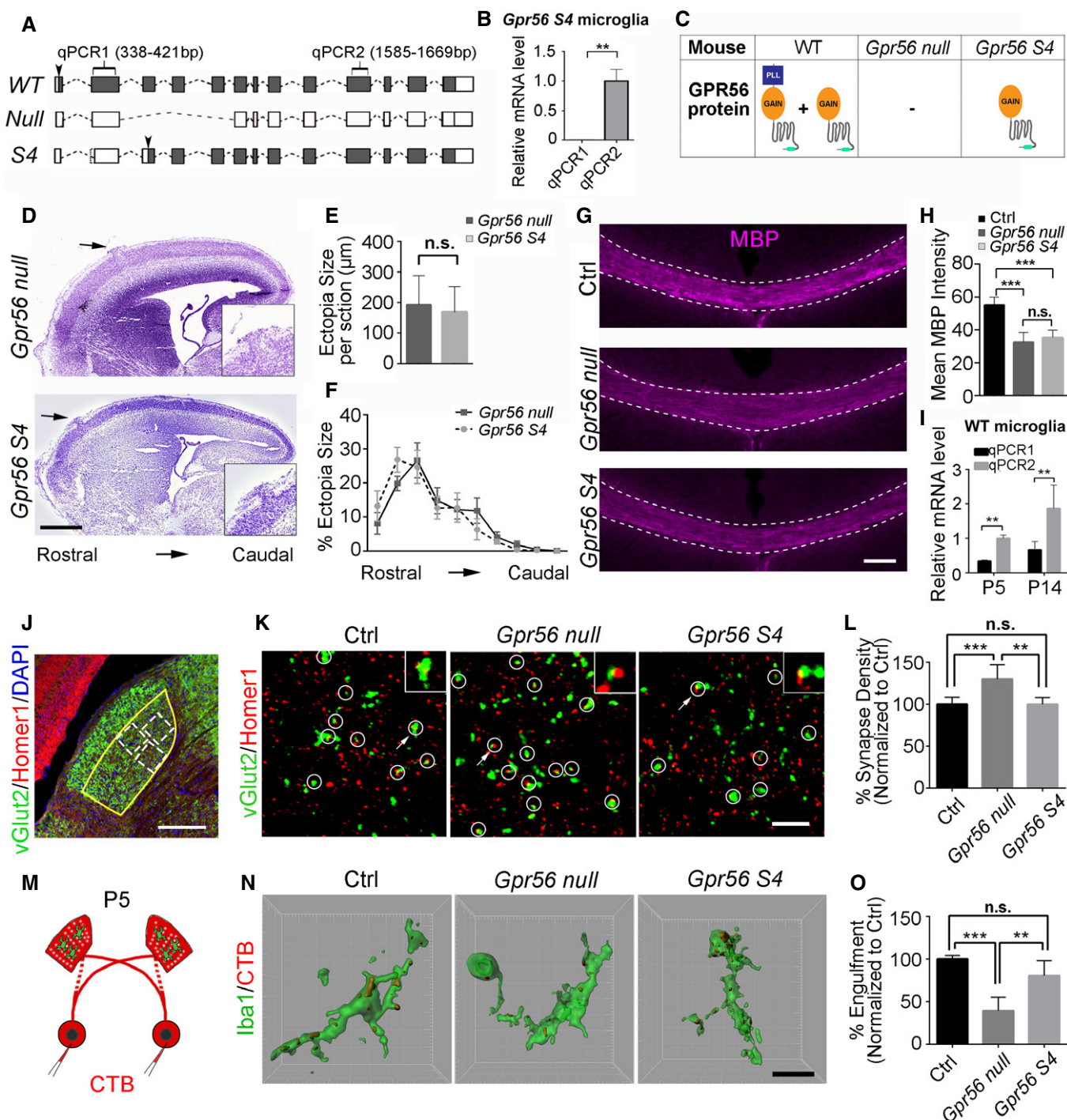


Figure 3.

**Figure 3. GPR56 S4 variant is required for synaptic refinement in the dLGN.**

- A A diagram showing *Gpr56* WT, null, and S4 transcripts. Solid boxes indicating exons that are transcribed. Arrowheads indicate the translation start sites.
- B *Gpr56* transcript levels in isolated microglia from *Gpr56* S4 mice.  $N = 3$ ,  $**P < 0.01$  by Student's *t*-test.
- C A table showing the expression status of *Gpr56* WT and S4 variants in microglia of different transgenic mice.
- D Representative images of Nissl staining of *Gpr56* null and *Gpr56* S4 E16.5 neocortex. Arrows indicate cortical ectopias that are shown in insets.
- E Quantification of ectopia size per section.  $N = 6$ ,  $P = 0.64$  by Student's *t*-test.
- F The distribution of ectopia from rostral to caudal cortex.  $N = 3$ ,  $F(9, 81) = 0.65$ ,  $P = 0.75$  by two-way ANOVA with Bonferroni's *post hoc* test.
- G Myelin basic protein (MBP) staining of corpus callosum in P28 controls, *Gpr56* null and *Gpr56* S4 mice. Scale bar, 100  $\mu$ m.
- H Quantification of MBP intensity in corpus callosum.  $N = 5$ ,  $***P < 0.001$  by one-way ANOVA with Tukey's *post hoc* test.
- I *Gpr56* transcript levels in WT microglia at P5 and P14.  $N = 4$ ,  $**P < 0.01$ , two-way ANOVA with Sidak's multiple comparisons test.
- J An overview of vGlut2 and Homer1 staining in dLGN at P10. The yellow outline indicates the dLGN core, and the dotted boxes show where synapses are quantified. Scale bar, 200  $\mu$ m.
- K Representative images of vGlut2/Homer1 staining in the dLGN of control, *Gpr56* null, and *Gpr56* S4 brains at P10. Arrows pointing to the enlarged synapse in the insets. Scale bar, 5  $\mu$ m.
- L Relative vGlut2/Homer1 synapse density in dLGN.  $N = 10$  (Ctrl),  $N = 6$  (*Gpr56* null),  $N = 3$  (*Gpr56* S4).  $**P < 0.01$ ,  $***P < 0.001$ , one-way ANOVA with Tukey's *post hoc* test.
- M A schematic representation of the *in vivo* engulfment assay. CTB are injected into both eyes at P4, and anterogradely trace RGC projections to the dLGN. After 24 h, the brains are collected and analyzed at P5.
- N Representative images and surface rendered microglia (green) in which CTB\* (red) RGC inputs were engulfed. Scale bar, 10  $\mu$ m.
- O Quantification of the percentage of engulfed RGC inputs in controls, *Gpr56* null and *Gpr56* S4 microglia.  $N = 4$ ,  $**P < 0.01$ ,  $***P < 0.001$ , one-way ANOVA with Tukey's *post hoc* test.
- Data information: Data are presented as mean  $\pm$  SEM in (F). For other statistics analysis, data are presented as mean  $\pm$  SD.

2016, 2017). Previous transmission electron microscopy (EM) studies estimated a distance of  $\sim 80$  nm between Homer1 and the presynaptic cleft (Dani *et al*, 2010) and a span from 0 to 200 nm between the vGlut2 vesicles and the presynaptic cleft (Fujiyama *et al*, 2004). In our analysis of 3D reconstructions of the SIM images, we defined a synapse when the distance from the center of a Homer1 immunoreactive spot to the nearest vGlut2 surface was between 0 and 300 nm (Movie EV1). Using this approach, we revealed that CKO mice had significantly increased synapse numbers compared to controls at P8 (Fig 4E and F, Appendix Fig S7). Importantly, SIM and confocal analyses yielded consistent synaptic changes (Fig 4D and F), supporting the usage of confocal imaging and analyses for other brain regions and transgenic mice.

Consistent with increased vGlut2<sup>+</sup>/Homer1<sup>+</sup> synapse numbers in CKOs, Western blot analysis of microdissected dLGN from P8 animals showed increased vGlut2 protein levels in CKOs as compared to control brains (Fig 4G and H), but no change in Homer1 protein levels (Fig 4I). It is worth noting that the increased synapse density was not the result of altered RGC number, since CKO had comparable brain-specific homeobox/POU domain protein 3A (Brn3a, a marker of RGC; Nadal-Nicolas *et al*, 2009) positive RGC density compared to controls (Fig EV4). Taken together, our data suggested that microglial GPR56 is important for normal synaptic refinement in dLGN.

To address whether the observed synaptic density increase was a consequence of a postnatal event, we generated animals that enabled inducible deletion of microglial *Gpr56* by crossing *Gpr56*<sup>fl/fl</sup> mice with *Cx3cr1-CreER* mouse line postnatally (Yona *et al*, 2013). *Gpr56*<sup>fl/fl</sup>; *Cx3cr1-CreER*<sup>+/-</sup> mice were used as inducible conditional knockouts (iCKO), and *Gpr56*<sup>+/-</sup>; *Cx3cr1-CreER*<sup>+/-</sup> mice were used as controls. Tamoxifen was administered to both iCKO and controls at P1-P3, and brains were analyzed at P10. We observed comparable increases in retinogeniculate synaptic density in both male and female iCKO mice, in comparison to their age-matched controls, indicating that there is no sexual dimorphism in microglial GPR56 function in the context of synaptic development (Fig 4J).

Furthermore, iCKO and CKO mice showed a quantitatively equivalent synapse phenotype at P10 (Fig 4D and J), indicating the observed synaptic phenotype is a postnatal event. Additionally, this result demonstrated that it is appropriate to use CKO mice for most of the remaining studies.

The dLGN also receives vGlut1<sup>+</sup> projections from neocortical layer VI (Fitzpatrick *et al*, 1994; Fujiyama *et al*, 2003; Thomson, 2010), which act as modulatory inputs that flexibly tune postsynaptic activity in target cells (Sherman & Guillery, 1996, 1998). In contrast to increased vGlut2<sup>+</sup> retinogeniculate synapses, there were no significant changes in the density of vGlut1<sup>+</sup> corticogeniculate synapses at P10 (Fig 4K–M), indicating that microglial GPR56 functions in a synapse-specific manner and does not modulate neocortical inputs in dLGN during the developmental stages investigated. Taken together, these findings demonstrate that microglial GPR56 is necessary for retinogeniculate synaptic development in early dLGN.

### Microglial GPR56 regulates hippocampal synaptic development

To address whether microglial GPR56 affects synaptic development in other brain regions, we examined synaptic density in the hippocampus at P10 and P21. In the hippocampus, Schaffer collateral axons from CA3 form synapse on CA1 pyramidal neurons exclusively on dendritic domains in the stratum (S.) oriens and S. radiatum (Swanson *et al*, 1978). Perforant path axons from the entorhinal cortex form synapses on CA1 region pyramidal neurons exclusively on dendritic domains in the S. lacunosum-moleculare, a critical neural circuit for temporal associative memory (Suh *et al*, 2011). We found increased synapse densities (vGlut2<sup>+</sup>/Homer1<sup>+</sup>) at both P10 and P21 in the hippocampal striatum lacunosum-moleculare layer (Fig 5A–D). However, we observed no change in vGlut1<sup>+</sup>/Homer1<sup>+</sup> synapse density at either P10 or P21 in hippocampus striatum radiatum layer (Fig 5E–H). Taken together, our data demonstrate that microglial GPR56 also plays an important role in hippocampal synapse development.

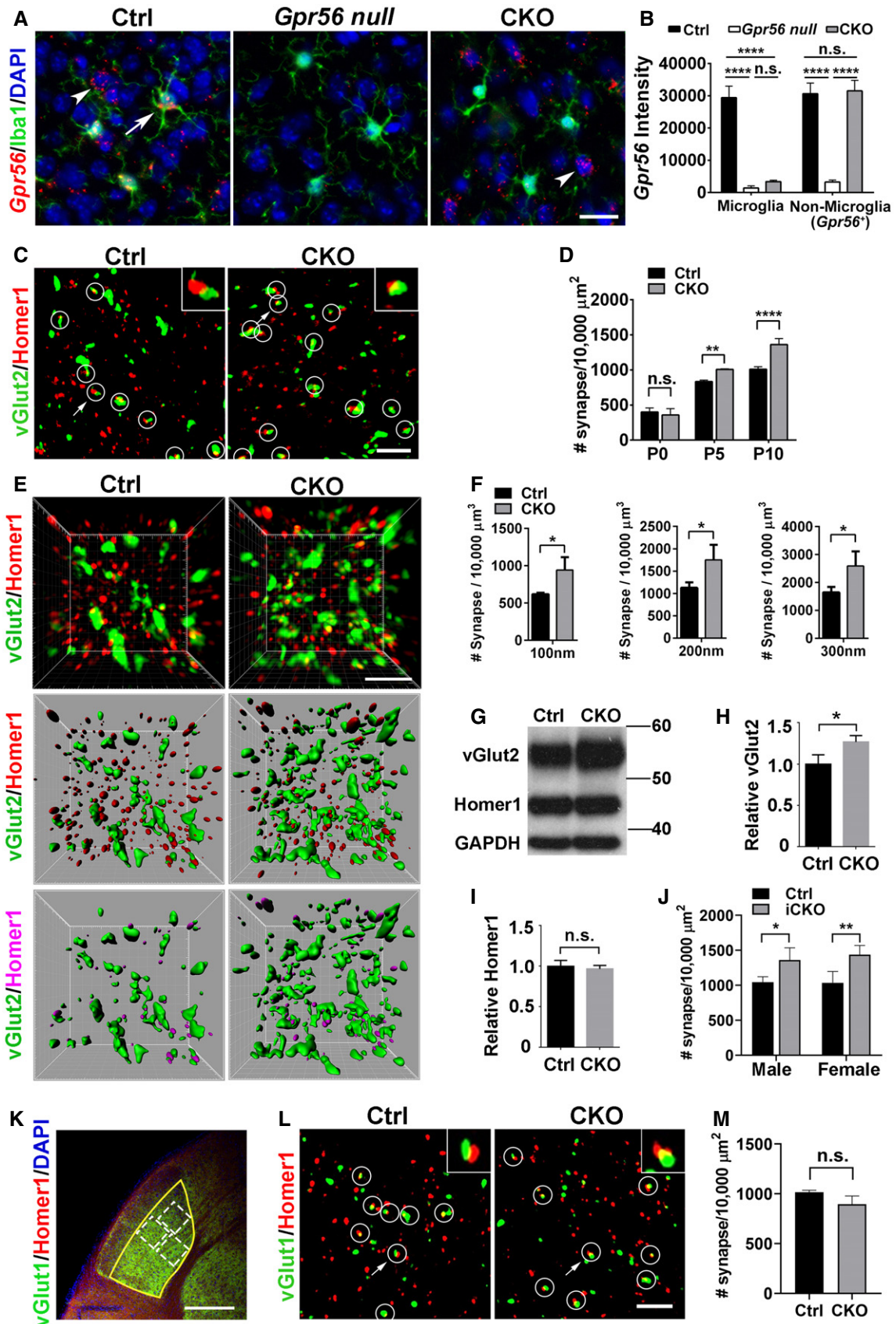


Figure 4.

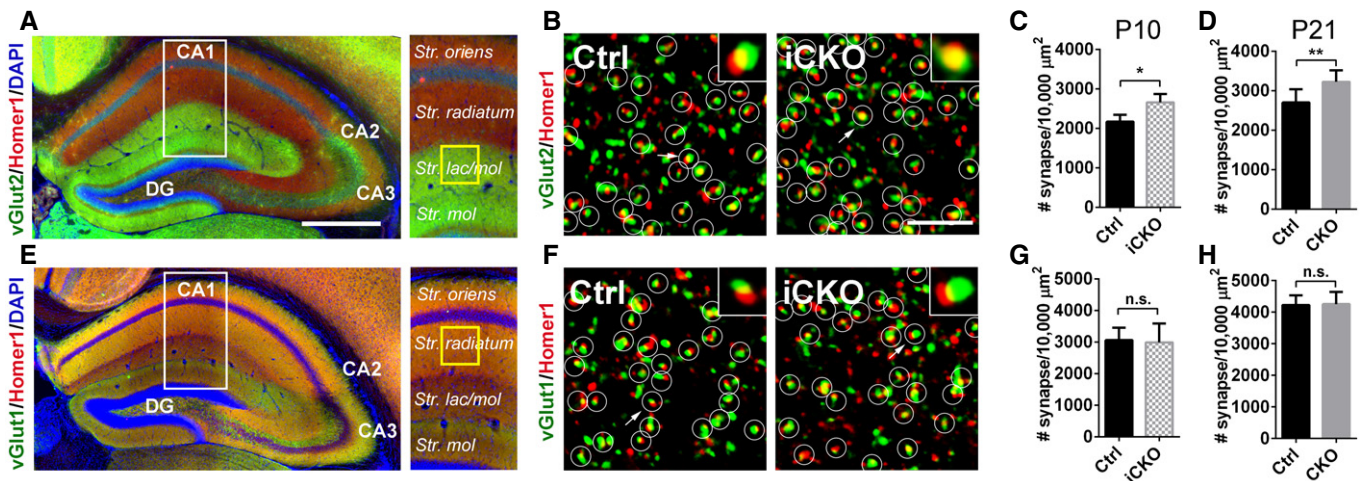


**Figure 4. Microglial GPR56 is required for synaptic development in the dLGN.**

- A *Gpr56* is deleted in CKO microglia. RNAscope shows *Gpr56* transcripts colocalize with microglia (arrow) in controls, but not in CKO, and is absent in all cell types in the global *Gpr56* KO (*Gpr56* null). Arrowhead indicates non-microglia cells expressing *Gpr56*. RNAscope was performed in the prefrontal cortex of P30 mice. Scale bar, 20  $\mu$ m.
- B Quantification of *Gpr56* fluorescence signals in (A).  $N = 20$ –50 cells for each.
- C Confocal images of vGlut2 (green) labeling retinal ganglion cell (RGC) presynaptic terminals and Homer1 (red) for postsynapses in the dLGN of CKO and controls at P10. Overlapped vGlut2 and Homer1 are quantified as synapses, indicated by white circles. Arrows pointing to the synapse enlarged in the upper right-hand inset. Scale bar, 5  $\mu$ m.
- D A time course of dLGN synapse density (vGlut2<sup>+</sup>/Homer1<sup>+</sup>) between WT and controls.  $N = 3$  for P0,  $N = 4$  for P5,  $N = 3$  for P10.
- E Representative super-resolution images and 3D-reconstructed images of vGlut2 and Homer1 staining of P8 dLGN. Green objects represent surface rendering of vGlut2<sup>+</sup> presynaptic terminals. Red spots are rendered Homer1<sup>+</sup> postsynapses. Magenta spots represent Homer1<sup>+</sup> postsynapses within a distance of 300 nm from the nearest vGlut2<sup>+</sup> surface. Scale bar, 2  $\mu$ m.
- F Quantification of Homer1<sup>+</sup> spots adjacent to vGlut2 surface within 100 nm, 200 nm, and 300 nm, respectively.  $N = 3$ .
- G Western blot of vGlut2 and Homer1 using microdissected dLGN tissue from P8 mice.
- H, I Quantification of vGlut2 and Homer1 expression in CKOs and controls.  $N = 3$ , \* $P = 0.027$ .
- J Quantification of synapse density (vGlut2<sup>+</sup>/Homer1<sup>+</sup>) in the dLGN of both male and female iCKO mice at P10.  $N = 3$  for male,  $N = 4$  for female.
- K An overview of vGlut1 and Homer1 staining in dLGN at P10. The yellow outline indicates the dLGN core, and the dotted boxes show where synapses are quantified. Scale bar, 200  $\mu$ m.
- L Representative images of vGlut1<sup>+</sup> (green) presynaptic terminals and Homer1<sup>+</sup> (red) postsynapses in the dLGN of CKO and controls at P10. Arrows pointing to the synapse enlarged in inset. Scale bar, 5  $\mu$ m.
- M Quantification of synapse density (vGlut1/Homer1) at P10 in the dLGN of CKO mice and controls.  $N = 3$  (WT),  $N = 5$  (CKO),  $P = 0.053$ .

Data information: \* $P < 0.05$ , \*\* $P < 0.01$ , \*\*\*\* $P < 0.0001$  using Student's *t*-test (F, H, I and M) or two-way ANOVA followed by Bonferroni's *post hoc* test (B, D and J). Data are presented as mean  $\pm$  SD.

Source data are available online for this figure.

**Figure 5. Microglial GPR56 is required for synaptic development in the hippocampus.**

- A Representative images show hippocampal vGlut2 and Homer1 immunostaining. White box outlines the region of interest and yellow box shows the regions where confocal images were taken. Scale bar, 500  $\mu$ m.
- B Confocal images of synaptic immunostaining in CA1 striatum lacunosum-moleculare (str. lac/mol) at P10. Arrows pointing to the enlarged synapse in the insets. Scale bar, 5  $\mu$ m.
- C, D Quantification of synapse density in CA1 str. lac/mol in iCKO versus control at P10 (C), and CKO versus control at P21 (D). At P10,  $N(\text{Ctrl}) = 4$ ,  $N(\text{iCKO}) = 3$ ,  $P = 0.02$ . At P21,  $N = 8$ ,  $P = 0.005$ .
- E Representative images show hippocampal vGlut1 and Homer1 immunostaining.
- F Confocal images of synaptic immunostaining in CA1 striatum radiatum at P10.
- G, H Quantification of synapse density in CA1 striatum radiatum in iCKO versus control at P10 (G), and CKO versus control at P21 (H). At P10,  $N = 5$ ,  $P = 0.83$ . At P21,  $N = 5$ ,  $P = 0.89$ .

Data information: \* $P < 0.05$ , \*\* $P < 0.01$ , Student's *t*-test. All data are presented as mean  $\pm$  SD.

**Increased synaptic density correlates with functional consequences**

During early postnatal periods, overlapping inputs from both eyes undergo a process of remodeling called eye-specific segregation,

resulting in the termination of ipsilateral and contralateral inputs in distinct non-overlapping domains in the mature dLGN (Sretavan & Shatz, 1984). Defective synaptic pruning of RGC inputs to the relay neurons in the dLGN leads to incomplete eye-specific segregation (Schafer *et al*, 2012; Chung *et al*, 2013; Vainchtein *et al*, 2018). To

investigate the effects of microglial GPR56 deficiency on eye-specific segregation, we performed anterograde tracing of RGC inputs with two different colored fluorescent CTB (Fig 6A) and quantified the extent of segregation with a threshold-independent method as described (Torborg & Feller, 2004; Tiriach *et al*, 2018). We observed a significantly larger overlap at P10 in CKO mice (Fig EV5A and B), persisting to P30 (Fig 6B–D) when eye-specific segregation should be completed, suggesting improper organization of retinogeniculate projections sustained throughout development.

To evaluate whether these excess synapses carry functional consequences, we examined the strength of the synaptic drive from RGCs to dLGN neurons by electrophysiological recordings. Whole-cell patch-clamp recordings from dLGN neurons were conducted in acute slices from either control or CKO mice at ~P30 (Fig 6E). When we examined maximal AMPA and NMDA receptor-mediated currents evoked by stimulation of the optic fibers that project to the dLGN, CKO mice displayed a significant increase in maximal NMDA receptor-mediated current (Fig 6F), consistent with an increase in overall number of retinal inputs onto dLGN relay neurons (Fig 4C–J) and increased NMDAR1 protein levels in Western blot analyses of microdissected dLGN from P30 CKOs compared to those from controls (Fig 6G and H). Mean maximal AMPA receptor-mediated currents were comparable between CKO and control mice (Fig 6I), consistent with a comparable GluR1 (an AMPA receptor subunit) protein level on Western blot (Fig 6J and K). Together, our data show microglial GPR56 is required for proper retinogeniculate circuit organization and function.

### Microglial GPR56 is required for the engulfment of PS<sup>+</sup> synapses

Our data so far showed significant increases in selected synapses in CKO mice. To investigate whether this change results from decreased synaptic pruning by microglia, we performed *in vivo* engulfment assay. Compared to controls, the engulfment of RGC material in CKO microglia was decreased by 25.7% (Fig EV5C and D). This change corresponded in magnitude to the increase in synapses at P5 (Fig 4D) and supports the hypothesis that a reduction in the engulfment of RGC inputs by *Gpr56*-deficient microglia led to the overall increase in retinogeniculate synapses.

Considering that PS binds GPR56 and flags RGC presynaptic inputs for removal by microglia, we further hypothesized that the elevated synapse numbers may have resulted from a reduction in microglial engulfment of PS<sup>+</sup> synapses. To test this hypothesis, we first examined the density of PS<sup>+</sup> RGC inputs by PSVue labeling in the P6 dLGN of both CKO mice and controls. As predicted, we observed a significantly higher percentage of RGC inputs that were colocalized with PSVue in CKO, compared to controls (Fig 7A and B). Considering the impaired ability to engulf synaptic elements by *Gpr56* CKO microglia (Fig EV5C and D), the increase of PS<sup>+</sup> RGC inputs in CKO dLGN might be a result of a decreased removal of PS<sup>+</sup> RGC inputs by CKO microglia. To test this hypothesis, we performed the modified microglial engulfment assay in CKO mice and their controls. Indeed, we found the engulfment of PS<sup>+</sup> RGC inputs was significantly decreased in CKO microglia, compared to controls (Fig 7C and D). In contrast, the engulfment of PS<sup>-</sup> RGC inputs was comparable between CKO and control microglia (Fig 7E). Of note, *Gpr56* CKO microglia still contained a low level of PS<sup>+</sup> RGC inputs, indicating that pathways other than GPR56 might

mediate this process. Taken together, our data support the notion that GPR56 specifically regulates engulfment of PS<sup>+</sup> synapses in microglia.

## Discussion

### Alternative splicing expands the functional repertoire of GPR56 in brain development

Cells use alternative splicing to expand their regulatory and functional capacity of genomes (Braunschweig *et al*, 2013). GPR56 is a well-suited example in this regard. *Gpr56 S4* is an alternative splicing isoform that includes a 5' deletion in exon 2, thus generating a new frameshifted transcript that uses a cryptic start site in exon 4 (Kim *et al*, 2010). As a consequence, the NTF of GPR56 S4 contains GAIN domain but lacks the PLL domain (Salzman *et al*, 2016), which mediates interactions with its two known extracellular ligands, collagen III, and TG2 (Yang *et al*, 2011; Luo *et al*, 2012; Salzman *et al*, 2016). Here, we uncover a distinct function of the GPR56 S4 isoform in microglia where it binds PS to mediate synaptic pruning. This discovery reveals a critical biological function for the GAIN domain. Prior to our work, the GAIN domain had been largely viewed as an aGPCR signature structure that mediates autolysis during protein maturation process.

### GPR56 regulates complex brain development in cell type-, isoform-, and ligand-specific manner

The adhesion GPCR (aGPCR) family, the second largest subfamily of GPCRs, consists of 33 members in the human genome (Hamann *et al*, 2015). Being a major class of matrix receptors, aGPCRs play essential functions in development by mediating cell–cell and cell–matrix interactions (Hamann *et al*, 2015). One of the most intensively studied aGPCRs associated with human developmental disorders is *GPR56*. Loss-of-function mutations in *GPR56* cause a devastating brain malformation called bilateral frontoparietal polymicrogyria (BFPP; Piao *et al*, 2004). MRI analyses of BFPP brains show compound malformation including cortical lamination defect and abnormal CNS myelination (Piao *et al*, 2004, 2005).

Microglia enter the developing brain prior to neural tube closure, where they proliferate and propagate along with the sequential processes of neurogenesis, synaptogenesis and pruning, and myelination (Reemst *et al*, 2016). Recent literature indicates that microglia play a key role in each step of brain development (Schafer *et al*, 2012; Parkhurst *et al*, 2013; Sato, 2015; Miyamoto *et al*, 2016; Hagemeyer *et al*, 2017). Microglial *Gpr56* expression is governed by a super-enhancer suggesting that it might be implicated in microglia core functions (Gosselin *et al*, 2014). This hypothesis is supported by the finding that *Gpr56* defines yolk sac-derived microglia (Bennett *et al*, 2018). In the present report, we provide insight into the functional significance of this expression pattern by showing that microglial GPR56 mediates synaptic pruning in multiple regions of the developing brain. Importantly, we show that an alternative splicing isoform, GPR56 S4, is responsible for microglia-mediated synaptic elimination by binding to PS, while the full-length GPR56 is required for its functions in cortical development by interacting with its ligand collagen III, and CNS myelination by mediating a

tripartite signaling with TG2 and laminin (Figs 3 and 8; Luo *et al*, 2011, 2012; Salzman *et al*, 2016; Giera *et al*, 2018).

As previously reported (Giera *et al*, 2015), loss of GPR56 led to defects in myelination (Fig 3G and H), which might impact synaptic pruning. However, in the developing visual system, myelination is

initiated after P7 and does not fully finish until P30 (Etxeberria *et al*, 2016; Mayoral *et al*, 2018). In contrast, synaptic pruning peaks at P5 and finishes around P10 in the dLGN. Here in *Gpr56* null mice, we observed the defect of synaptic pruning as early as P5 (Fig 3N and O), which occurred before myelination initialization. Based on

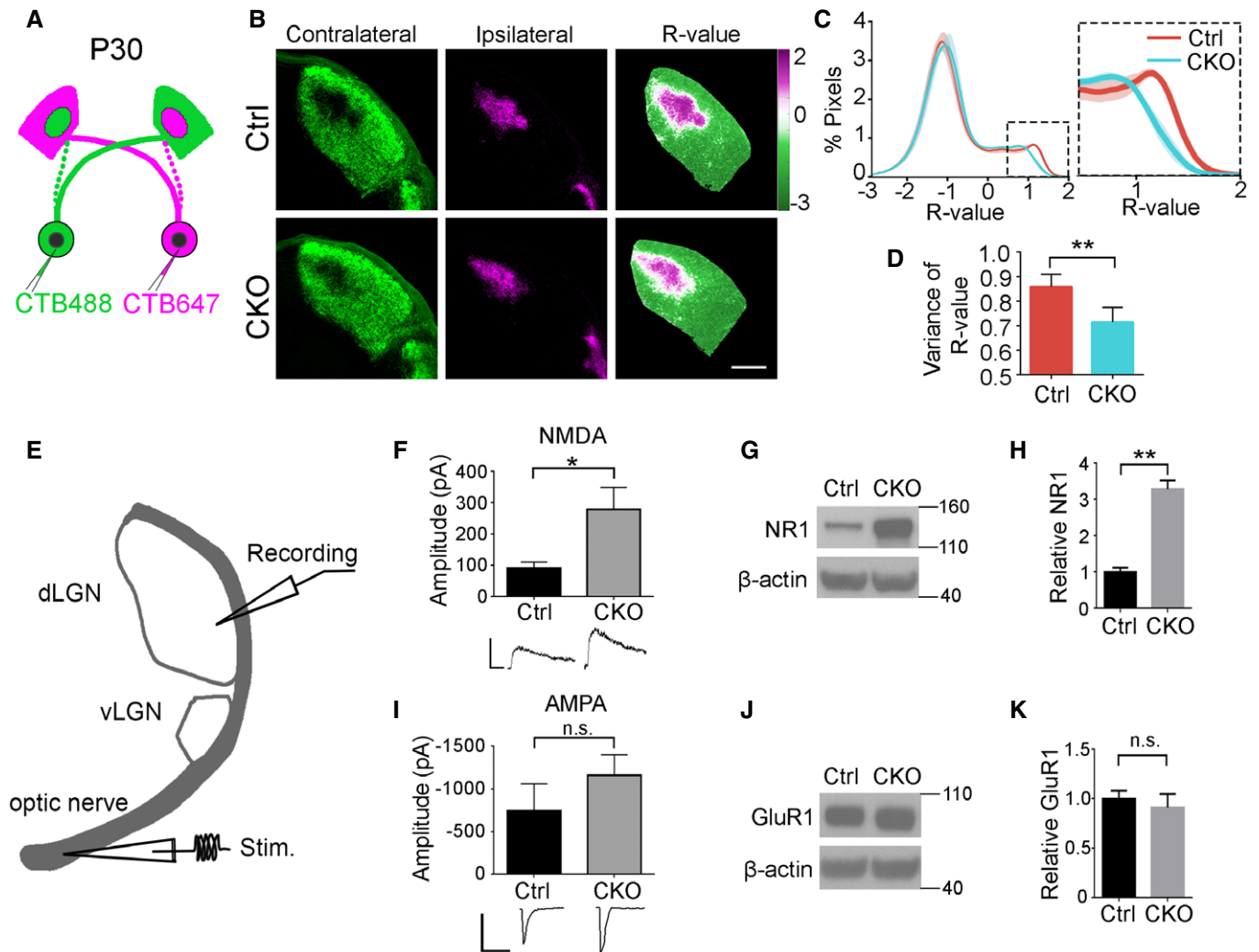


**Figure 6. Microglial *Gpr56* deficiency leads to impaired retinogeniculate circuit organization and function.**

A A diagram of eye-specific segregation assay at P30.

B CTB-labeled dLGN shows reduced eye segregation at P30 in CKO mice. The left column shows contralateral dLGN labeled with CTB488 (green), and the middle one is ipsilateral dLGN with CTB647 (magenta). The right column represents the dLGN pseudocolored according to the R-value for each pixel ( $R = \log(F_{\text{ipsi}}/F_{\text{contra}})$ ). Scale bar, 200  $\mu\text{m}$ .

C A histogram distribution chart of R-value for all pixels within dLGN represents the degree of eye-specific segregation. When R is 0, it means equal ipsilateral and contralateral fluorescence intensity at a pixel. A greater R-value means a bigger difference of ipsi- to contra-lateral fluorescence intensity. The narrower distribution of CKO in the inset indicates reduced segregation.

D The variance of R distributions in P30 control and CKO mice.  $N = 4$  (Ctrl),  $N = 6$  (CKO),  $P = 0.004$ , mean  $\pm$  SD.

E A schematic diagram of electrophysiological recording in a parasagittal dLGN.

F Maximal NMDAR-mediated currents measured in the dLGN of P28–P34 mice,  $P = 0.03$ ,  $N = 14$  (Ctrl), 23 (CKO) cells from 5, 7 mice, respectively. Mean  $\pm$  SEM.

G Western blot of NMDAR1 (NR1) using microdissected dLGN tissue from P30 mice.

H Quantification of NMDAR1 expression in CKO mice and control.  $N = 3$ ,  $P = 0.007$ , mean  $\pm$  SD.

I Maximal AMPAR-mediated currents measured in the dLGN of P28–P34 mice.  $P = 0.302$ ,  $N = 13$  (Ctrl), 17 (CKO) cells from 5, 7 mice, respectively. Mean  $\pm$  SEM.

J Western blot of GluR1 with microdissected P30 dLGN tissue.

K Quantification of GluR1 expression in CKO mice and controls.  $N = 3$ ,  $P = 0.40$ , mean  $\pm$  SD.

Data information: \* $P < 0.05$ , \*\* $P < 0.01$ , Student's *t*-test.

Source data are available online for this figure.

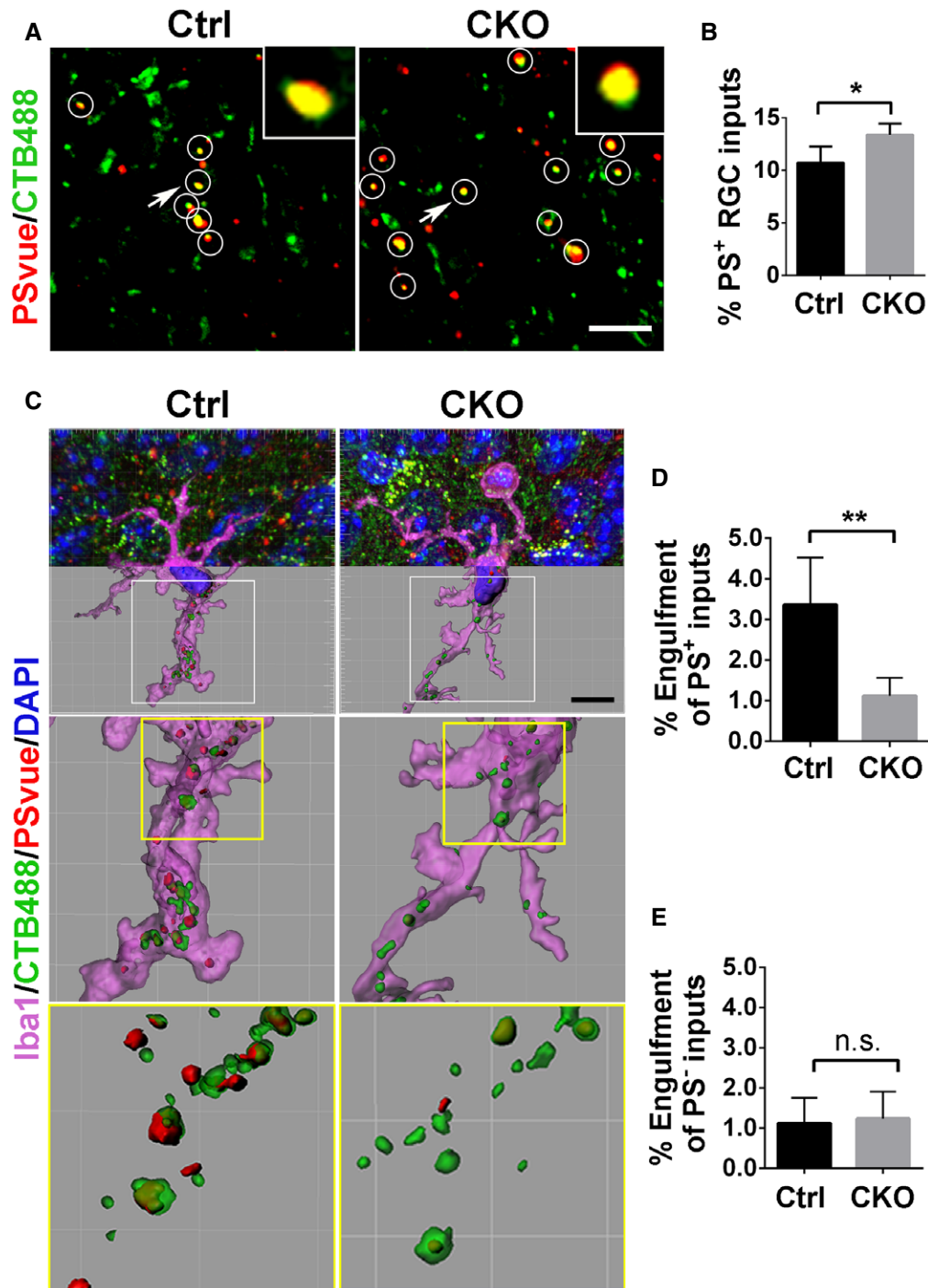


**Figure 7. Deletion of microglial GPR56 causes decreased engulfment of PS<sup>+</sup> RGC inputs.**

**A** Colocalized RGC inputs and PSVue signals in P6 control and CKO. White circles indicate PS<sup>+</sup> RGC inputs. Arrows pointing to the RGC inputs enlarged in the insets. Scale bar, 5  $\mu$ m.

**B** The percentage of PS<sup>+</sup> RGC inputs in total inputs in CKO and controls.  $N = 5$ ,  $*P = 0.02$ .

**C** Representative images of engulfed PS<sup>+</sup> and PS<sup>-</sup> RGC inputs by microglia in control and CKO. Scale bar, 10  $\mu$ m.

**D** Quantification of engulfed PS<sup>+</sup> RGC inputs by microglia, which is calculated as follows: Volume of engulfed PS<sup>+</sup> RGC inputs/Volume of microglia cell.

**E** Quantification of engulfed PS<sup>-</sup> RGC inputs in control and CKO.

Data information:  $N = 4$  (Ctrl),  $N = 5$  (CKO),  $**P = 0.005$  in (D),  $P = 0.80$  in (E).  $*P < 0.05$ ,  $**P < 0.01$ , Student's  $t$ -test. Data are presented as mean  $\pm$  SD.

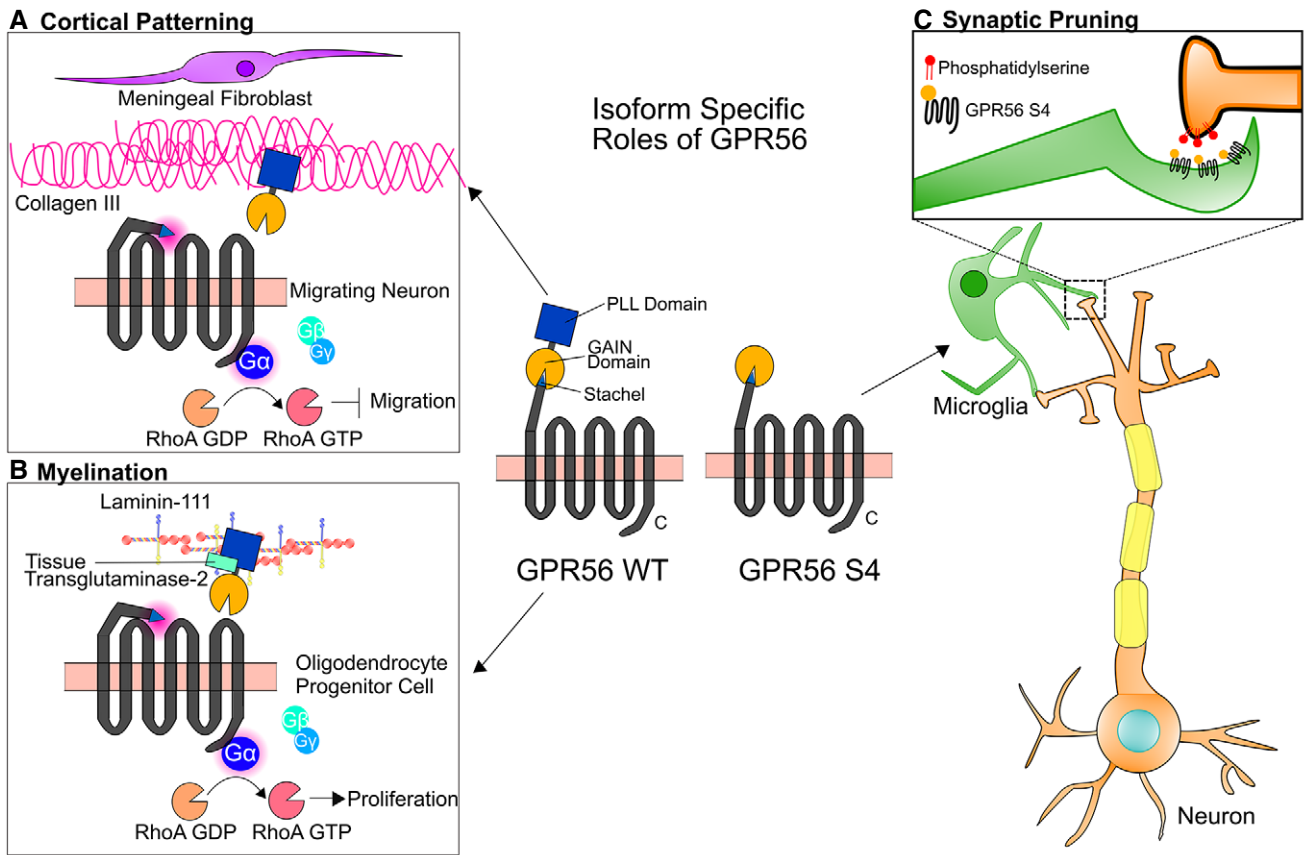


**Figure 8. Isoform-specific roles of GPR56 in the brain.**

The NTF of WT GPR56 contains both PLL and GAIN domains. The S4 variant of GPR56 contains only the GAIN domain.

- A WT GPR56 participates in cortical patterning during brain development. Collagen III, secreted by meningeal fibroblasts, activates GPR56 by binding to its PLL domain and sends a stop signal to migrating neurons once they reached to the pial basement membrane (Luo *et al*, 2011).
- B In oligodendrocyte progenitor cells (OPCs), WT GPR56 binds to microglia-secreted tissue transglutaminase-2 (TG2) in the presence of laminin-111 to promote OPC proliferation (Giera *et al*, 2015, 2018).
- C In microglia, GPR56 S4 binds to externalized PS, which services as an “eat-me” signal for those synapses needed to be removed, and mediates the engulfment of synapses by microglia.

these, it is unlikely that myelination defects impact synaptic pruning in this context.

#### Exposed PS serves as an “eat-me” signal for synapses to be engulfed by microglia

Under normal conditions, PS is mainly restricted to the inner leaflet of the cell membrane. When cells undergo apoptosis, PS is exposed to the outer surface of the cell. This PS externalization is regulated by flippase and scramblase (Zachowski *et al*, 1989; Nagata *et al*, 2016). Caspases can inactivate flippase and activate scramblase at the plasma membrane by cleavage and induce apoptotic PS externalization (Segawa & Nagata, 2015). Thus, exposed PS has become a classic “eat-me” signal for macrophage/microglia to phagocytose apoptotic cells.

It has been postulated that synapses could undergo focal apoptosis and be cleared. *In vitro* data showed that key characteristics of apoptosis, including PS externalization and caspase activation, were exhibited on cortical synaptosomes and on dendrites in cultured

hippocampal neurons upon treatment of apoptosis inducer, like Staurosporine and  $Fe^{2+}$  (Mattson *et al*, 1998). Additionally, it has been shown that activated caspase-3 was colocalized with C1q on synapses in the brain tissue (Gyorffy *et al*, 2018) and that the focal activation of caspase-3 caused dendrite retraction and spine elimination without killing the neuron (Erturk *et al*, 2014). Thus, current literature supports that a focal apoptotic mechanism might underlie the synaptic pruning. However, there has been no report on the presence of  $PS^+$  synapses *in vivo*.

Here, for the first time, we demonstrate externalized PS on synapses *in vivo*, which strongly supports the focal synaptic apoptosis hypothesis. In the developing mouse visual system, we detected ~10% of RGC synaptic inputs were  $PS^+$  at P6, an active period of microglia-mediated synaptic pruning; and much fewer  $PS^+$  inputs were found at P13, when synaptic pruning was essentially completed in the dLGN (Fig 1C and D). This finding indicates that synapses intended to be removed expose PS as an “eat-me” signal to enable a targeted removal by microglia. We further strengthened this notion by revealing that over 70% RGC synaptic inputs

engulfed by microglia were PS<sup>+</sup>, in contrast to 27% of PS<sup>-</sup> RGC inputs (Fig 1K). Taken together, our data support that exposed PS serves as an “eat-me” signal for synapses to be engulfed by microglia.

### GPR56 functions as a PS receptor

We uncover a new direct PS-binding protein, the S4 isoform of GPR56. Several different PS-recognizing membrane receptors have been identified under the categories of either direct PS receptors and indirect opsonin-based PS receptors (Bever & Williamson, 2016). For example, BAI1 (Park *et al*, 2007), Tim-4 (Miyaniishi *et al*, 2007), and Stabilin-2 (Park *et al*, 2008) are direct PS receptors, whereas TAM receptors (Tyro3, Axl, and MerTK) bind PS via GAS6 and Protein S (Ohashi *et al*, 1995; Stitt *et al*, 1995; Mark *et al*, 1996; Nagata *et al*, 1996; Lemke, 2013). Most of these receptors are related to engulfment of apoptotic cells. One intriguing question is whether these PS receptors also mediate engulfment of synapses. Indeed, our present study demonstrates that PS-binding protein GPR56 promotes the engulfment of PS<sup>+</sup> synapses by microglia. Interestingly, we found CKO microglia still engulf some PS<sup>+</sup> synapses (Fig 7C and D), indicating there might be other molecular pathways that regulate engulfment of the remaining PS<sup>+</sup> synapses.

Another provocative question is how GPR56 functions together with other PS receptors in regulating developmental synaptic pruning. One possible scenario is that various PS receptors function in concert to prune synapses, as observed in microglia engulfment of dying neurons where BAI1 regulates the formation of phagosomes around dying neurons and Tim-4 controls phagosome stabilization (Mazaheri *et al*, 2014). Another possibility is that different cell types use different PS receptors. In supporting the second possible scenario, single-cell RNA-seq database reveals that BAI1 and MEGF10 are highly expressed in astrocytes, but barely detectable in microglia, GPR56 and MERTK are expressed in both microglia and astrocyte, whereas Tim-4 and Stabilin-2 are minimally detectable in microglia and astrocyte (Zhang *et al*, 2014).

### Concluding remarks

Defective synapse pruning has been implicated in autism spectrum disorder (Tang *et al*, 2014), whereas excessive synapse removal has been linked to schizophrenia (Sekar *et al*, 2016; Sellgren *et al*, 2019). Insight into the mechanisms underlying synapse refinement during development will help decipher neurodevelopmental disorders linked to synapse imbalance. Key unanswered questions include how synapses destined for removal externalize PS and whether GPR56 functions independently or in concert with complement components in microglia-mediated synaptic pruning. Given its high expression in adult microglia (Matcovitch-Natan *et al*, 2016), our data also raise a broader question of whether microglial GPR56 has any role in adult synapse homeostasis. Given its multifarious and cell type-specific roles in neurodevelopment (Folts *et al*, 2019), further study of GPR56 function in synaptic pruning represents an attractive opportunity to integrate this process into other aspects of brain wiring including myelination. This understanding will promote the objective of enabling therapeutic targeting of GPR56 for combating neurodevelopmental and neurodegenerative disorders.

## Materials and Methods

### Animals

All mice were handled according to the guidelines of Animal Care and Use Committee at Boston Children’s Hospital and University of California, San Francisco. *Gpr56<sup>fl/fl</sup>* mice were generated as previously described (Giera *et al*, 2015). The *Cx3Cr1-cre* (B6J.B6N (Cg)-*Cx3cr1<sup>tm1.1(cre)Jung/J</sup>*, #025524) and *Cx3Cr1-creER* (B6.129P2 (Cg)-*Cx3cr1<sup>tm2.1(cre/ERT2)Litt/WganJ</sup>*, #021160) mice were obtained from Jackson Laboratories. Considering both *Cx3Cr1<sup>Cre</sup>* and *Cx3Cr1<sup>CreER</sup>* are knock-in mice, we crossed these mice with *Gpr56<sup>fl/fl</sup>* to generate *Gpr56<sup>fl/fl</sup>;Cx3Cr1-cre (or creER)<sup>+/-</sup>* as conditional knock-out mice, and *Gpr56<sup>+/+</sup>; Cx3Cr1-cre (or creER)<sup>+/-</sup>* as controls. CreER is a tamoxifen-inducible Cre recombinase. To induce a deletion of microglial *Gpr56*, 40 µg tamoxifen (in corn oil, Sigma) per day for three consecutive days (P1–P3) were given to neonatal animals via intraperitoneal injection (Parkhurst *et al*, 2013). To generate *Gpr56 null* mice, *Gpr56<sup>fl/fl</sup>* mice were crossed with *CMV-cre* mice (JAX stock #006054) (Schwenk *et al*, 1995) to delete exons 4–6, causing a deletion of *Gpr56* in all tissues. Rosa<sup>GFP</sup> reporter mice were made from pR26 CAG/GFP vector (Plasmid #74285, Addgene), which contains a loxP-flanked STOP cassette and a GFP reporter, which is expressed under the control of an IRES. Then, the vector was micro-injected into C57BL/6 zygotes to make transgenic mice via CRISPR/Cas9 strategy in the Transgenic Core Laboratory of Boston Children’s Hospital (Chu *et al*, 2016).

### Immunohistochemistry

Mouse brains were collected following PBS perfusion and fixation with 4% PFA and cryoprotected in 30% sucrose. OCT-embedded tissues were cryosectioned at 14 µm or 40 µm. For immunostaining, 14-µm or 40-µm sections were incubated with blocking buffer (10% Goat serum + 1% BSA; 0.3% Triton-X/PBS) for 2 h and stained with primary antibodies overnight at 4°C (guinea pig anti-vGlut2, 1:1000, Millipore AB2251-I; guinea pig anti-vGlut1, 1:1,000, Millipore AB5905; rabbit anti-Homer1, 1:250, Synaptic Systems, 160 003; rabbit anti-Iba1, 1:250, Wako 019-19741; guinea pig anti-Iba1, 1:500, Synaptic Systems 234 004; rat anti-CD68, 1:250, AbD Serotec MCA1957; rat anti-MBP, 1:100, Abcam ab7349), followed by fluorophore-conjugated secondary antibodies for 2 hours at room temperature. Tissues were mounted with Fluoromount-G (Southern Biotech, 0100-01) or Vectashield antifade mounting medium (Vector Laboratories, H-1000).

### In vivo phosphatidylserine labeling

P5 mice were given an intraocular injection of CTB647 into both eyes. Twenty-four hours later, mice were mounted on a neonatal mice adaptor (RWD Life Science, #68072), and given an intracranial injection of various labeling probes. The stereotaxic setting was –1.5 mm anteroposterior, 1.09 mm mediolateral, and –2.15 mm dorsoventral to lambda. 2 µl PSVue (20 µM in TES buffer, Millipore Sigma T1375) or pSIVA(1:2, 2 mM Ca<sup>2+</sup> in HBSS) was injected into the gap area between hippocampus and dLGN via a 33G needle attached Hamilton syringe at 0.33 µl/min (see Fig EV1A and C). Six hours later, brains were collected

freshly and sectioned at 180  $\mu\text{m}$  in ice-cold TES buffer or 1 mM  $\text{Ca}^{2+}$  HBSS on the vibratome (Leica VT1000 S). Two to three sections with medial dLGN were chosen and directly mounted on homemade framed (concave, 200  $\mu\text{m}$  depth) glass slides. The images were taken immediately within an hour on a Zeiss LSM700 confocal microscope at 63 $\times$ .

### **In vivo engulfment**

*In vivo* engulfment assay was carried out as previously described (Schafer et al, 2012). Briefly, P4 mice were given an intracocular injection of 0.5  $\mu\text{l}$  0.5% CTB594 into each eye 24 h prior brain collection. 40  $\mu\text{m}$  cryosections were obtained for the assay. 2–3 sections of medial dLGN were chosen from each mouse for further free-floating immunostaining with Iba1 antibody. Images were taken on a UltraView Vox spinning disk confocal microscope at 60 $\times$  with 0.2  $\mu\text{m}$  z-step or on a Zeiss LSM700 confocal microscope at 63 $\times$  with 0.2  $\mu\text{m}$  z-step. ImageJ (NIH) and Imaris (Bitplane) were used for image processing. 3D reconstruction of microglia and RGC inputs was created by surface rendering in Imaris. To enable quantitative assessment of engulfment, and to control for variation in microglia volume, we calculated the engulfment percentage as follows: Volume of internalized RGC inputs/Volume of microglia. To quantify the engulfment of  $\text{PS}^+$  or  $\text{PS}^-$  RGC inputs, the following formula was used: % Engulfment of  $\text{PS}^+$  or  $\text{PS}^-$  RGC inputs = Volume of internalized  $\text{PS}^+$  or  $\text{PS}^-$  inputs/Volume of microglia.

### **Generation of GPR56 fusion proteins**

Human IgG Fc-tagged constructs were generated by PCR. For GPR56 NTF-hFc, the PCR forward primer is as follows: 5'-CCATGGAAGACTTCCGCTTCTGTGGCC-3', the reverse primer is as follows: 5'-CAGATCTCAGTGGTTGCACAGGCAGG-3'. For GPR56 GAIN-hFc, the PCR forward primer is as follows: 5'-ATCCATGGTTATGTG TGATC TCAAGAAGGAATTGC-3', the reverse primer is as follows: 5'-TCTAGATCTCAGTGGTTGCACAGGCAGG-3'. Then, PCR product was inserted into pFUSE-hlgG2-Fc2 (InvivoGen, Cat. pfuse-hfc2) vector between Nco1 and BglII sites. For the expression of GPR56 fusion proteins, the above constructs were transiently transfected into HEK-293T cells (ATCC). 24 h later, the culture media was changed to serum-reduced Opti-MEM (Gibco, 31985070). During incubation, GPR56 fusion proteins would be secreted into the culture media. This conditioned media containing fusion proteins was harvested 48–72 h later and concentrated as previously described (Li et al, 2008). The proteins were purified using HiTrap protein A column (GE Healthcare, 17040303).

### **Flow cytometry**

GPR56 NTF-hFc, GAIN domain-hFc, or hFc were labeled with Alexa Fluor 647 (AF647) using the Alexa Fluor 647 NHS Ester labeling kit (Thermo Fisher Scientific, Cat #A20006) according to the manufacturer's protocol. Briefly, 75  $\mu\text{M}$  protein was incubated with 300  $\mu\text{M}$  AF647 at room temperature for 4 h, followed by 200 mM Tris to quench the reaction. The whole reaction mixture was run through a Sephadex G-50 column and protein–dye conjugate was collected. Dye labeling efficiency for each protein ranged from 1.44 to 1.46 moles of dye per mole of protein.

Ba/F3 cell line was cultured and passaged as described (Cermak et al, 2016). It was maintained in RPMI-1640 media with L-glutamine (Invitrogen, Cat #11875093) supplemented with 10% FBS, penicillin–streptomycin, and kept at 37°C, 5%  $\text{CO}_2$  in a humidified incubator. Cells were harvested and washed twice with ice-cold Hank's balanced salt solution (HBSS) and resuspended in HBSS. Cells were treated with 1  $\mu\text{M}$  calcium ionophore A23187 (Millipore Sigma, Cat #C7522) at 37°C for 15 min, with gentle agitation every 5 min, followed by washing with HBSS. To measure direct binding, cells were resuspended in 0.9% NaCl and incubated with 1  $\mu\text{M}$  protein-Alexa Fluor 647 conjugate at room temperature for 2 h. After binding, cells were washed once and resuspended in HBSS, followed by flow cytometry on an LSRFortessa (BD Biosciences). For the competition assay, cells were treated with A23187 as above and washed with HBSS. Next, cells were resuspended in 100  $\mu\text{l}$  staining buffer (10 mM HEPES, 140 mM NaCl, 2.5 mM  $\text{CaCl}_2$ , pH 7.4) and incubated with 1  $\mu\text{M}$  AF647-conjugated NTF, GAIN, or hFc and 50 nM Annexin V-FITC for 1 h at room temperature. Cells were washed once with HBSS, followed by flow cytometry on an LSRFortessa (BD Biosciences). Ba/F3 cell line was a gift from the Manalis laboratory at Massachusetts Institute of Technology.

### **Protein lipid overlay assay**

The membrane lipid strips (Echelon Biosciences, Inc.) were blocked in 3% fatty acid-free BSA and 1% fatty-free milk in 0.1% Tween-20 TBS for 1 h at room temperature. The membrane was then incubated in 3% BSA containing 3  $\mu\text{g/ml}$  purified human Fc-tagged GPR56-GAIN domain (hFc-GAIN) at 4°C with gentle agitation. After three times wash, the strips were incubated with goat anti-human IgG Fc HRP-conjugated secondary antibody for 1 h (Thermo Fisher Scientific). The film was exposed following routine immunoblotting steps. The whole experiment was processed in the dark, because this lipid strips were sensitive to light.

### **QPCR**

RNA of microglia was isolated using the miRCURY™ RNA isolation kit (EXIQON, Cat. #300110) and was reverse-transcribed using a kit of SuperScript™ IV VILO™ Master Mix with ezDNase (Invitrogen, Cat. # 11766050). CDNA was used as template for PCR reactions with LightCycler® 480 SYBR Green I Master (Roche, Cat. # 04707516001) in a Roche LightCycler® 480 II machine. Forward and reverse primers for qPCR1 (338-421) are 5'-CGGGCAGATGGTCTACTTCCT-3' and 5'-AAGCGGAAGTCTTCTCGGGG-3', respectively. Forward and reverse primers for qPCR2 (1585–1669) are 5'-TTGCTGCCTACCTCTGTCC-3' and 5'-AGCAGGAAGACAGCGGACAG-3', respectively.

### **Synapse quantification**

Confocal microscopy images were obtained with Zeiss LSM 700 System. For synapse quantification in dLGN, medial dLGN slices were used. In each dLGN, three fields of view (5 serial optical sections, 0.5  $\mu\text{m}$  Z-step, 101.5  $\mu\text{m}$  \* 101.5  $\mu\text{m}$ , 1,024  $\times$  1,024 pixel) were acquired in the upper part of the core region using a 63 $\times$ /1.40 oil objective. Colocalization of vGlut2/Homer1 or vGlut1/Homer1

was quantified as described (Lehrman *et al*, 2018). The whole process was run in the ImageJ software (NIH, Bethesda, MD). First, each channel's background was subtracted with a rolling ball radius of 10 pixels. Then, thresholding was properly applied to each channel to distinguish synaptic puncta from background and generate two new binary images. To detect the overlay of pre- and postsynaptic puncta, a logical operation "AND" was performed between these two images. Lastly, the overlaid puncta were counted as synapse using the "analyze particles" function. The full code can be found at [https://github.com/TaoLi322/Microglia\\_GPR56\\_Synapse/blob/master/Synapse-quantification](https://github.com/TaoLi322/Microglia_GPR56_Synapse/blob/master/Synapse-quantification). All images were acquired and analyzed blindly.

For super-resolution imaging of synapses, a modified version of the protocol in Hong *et al* (2017) was employed. In brief, imaging was performed using a Zeiss ELYRA PS1 structured illumination microscopy (SIM). Tissue was mounted with Prolong Gold (Invitrogen P36934) and covered by High Precision Cover Glass (1.5H, Azer scientific). Sections were imaged at 90 nm Z-step using a 100× oil-immersed objective lens. Images were processed using the Zen image software (Carl Zeiss) and then inputted into Imaris for 3D rendering and analysis. The vGlut2 channel was processed using surface rendering function, and Homer1 channel was processed with the spot function. A MatLab program "spot to surface" was applied to count the number of adjacent Homer1 spots to vGlut2 surface ( $\leq 100$  nm, 200 nm, and 300 nm distance from spot centers to surface).

### RNAscope

RNAscope was performed using RNAscope<sup>®</sup> Multiplex Fluorescent Reagent Kit v2 for fixed and frozen 12 μm thick sections according to the manufacturer's instructions. RNAscope<sup>®</sup> Probe-Mm-*Gpr56* (Cat No. 318241) was used to detect expression of the C-terminal target region of *Gpr56* followed by immunohistochemistry for Iba1 (1:400, Wako, 019-19741). In short, after signal amplification step for *Gpr56*, sections were permeabilized using 0.3% Triton-X 100 in PBS for 10 min, followed by blocking with 10% goat serum, 1% BSA and 0.1% Triton-X 100 in PBS for 1 h at RT and incubating the primary antibody Iba1 in the blocking buffer overnight at 4°C. Appropriate secondary antibody was used to visualize Iba1 expression.

### Western blot of dLGN

Mice (P30) were anesthetized and decapitated. Mouse brains were immediately removed into ice-cold HBSS and coronally sectioned at 200 μm using vibratome. DLGN were dissected out under dissection microscope and homogenized in proteinase inhibitor-added RIPA buffer. After 30min incubation on ice, samples were centrifuged at 14,000 g for 10 min. Supernatant was collected and used for WB of NMDAR1 (anti-NR1, 1:2,000, Sigma-Aldrich 05-432) and vGlut2 (anti-vGlut2, 1:5,000, Millipore AB2251-I). For WB of GluR1 (anti-GluR1, 1:1,000, Cell signaling 13185S), supernatant was boiled for 5 min before loading.

### Microglia cell isolation

Microglia were isolated from whole brains without cerebellum using a modified Percoll gradient assay (Frank *et al*, 2006). The whole

process was carried out under ice-cold conditions, unless other temperatures were used. Briefly, anesthetized mice were perfused with ice-cold Hank's balanced salt solution (HBSS). The fresh brains were immediately minced into 1–2 mm chunks using a clean razor blade and transferred to a Dounce homogenizer. Using a loose glass pestle, brain tissues were gently homogenized with around 15 strikes, until large chunks had dissociated. Then repeat the homogenization with a tight pestle until the tissue had been mostly dissociated to single cells. The cell suspension was pelleted at 300 g for 7 min. The cell pellets were resuspended in 5 ml of 70% Percoll (GE Healthcare, Cat. # 17089101) diluted in HBSS. Another layer of 5 ml 37% Percoll was gently added on top of the cell suspension layer. Then it was spun at 800 g, 22°C for 25 min, with the acceleration rate setting at 5 and deceleration rate at 1. A thin, cloudy layer of cells at the interface was carefully collected and pelleted. These cells were used for following Western blot of microglia.

The cells were resuspended in FACS buffer (0.2% BSA in HBSS), and stained with CD11b-PE (BD, Cat. #553311) and CD45-BV421 (BD Horizon™, Cat. #563890) at a 1:100 dilution for 20 min. The cells were then washed and spun down at 300 g for 7 min. The samples were resuspended again in FACS buffer containing DRAQ7 (Abcam, cat. #ab109202) at a 1:100 dilution and filtered through a 35 μm cell strainer. Using a BD FACSAria II sorter, CD11b<sup>+</sup>, CD45<sup>low</sup>, DRAQ7<sup>-</sup> cells were collected as microglia, which were further used for qPCR experiments.

### Eye-specific segregation

Threshold-independent analysis of eye-specific segregation was performed as described before (Torborg & Feller, 2004). Mice were anesthetized with isoflurane during the whole procedure. 3 μl 0.2% cholera toxin B subunit (CTB)-conjugated Alexa 488 dye (CTB488, Life Technologies, C22841) was intravitreally injected into the left eye, and CTB-conjugated Alexa 647 dye (CTB647, Life Technologies, C34778) into the right eye of P30 mice. 24 hours later, mice were transcardially perfused with PBS and fixed with 4% PFA, and cryoprotected in 30% sucrose. The injection/labeling efficiency was checked by visualizing retinas and superior colliculus (Appendix Fig S8A). Brains were cryosectioned coronally at 60 μm and mounted with Fluoromount-G (SouthernBiotech). Since variance of R-value varies much from cranial to caudal LGN (Tiriach *et al*, 2018), we chose three to four dLGN (420–600 μm from caudal LGN) as indicated in (Appendix Fig S8B) for analysis. 16-bit images were digitally acquired at 20× with a CCD camera (Nikon eclipse Ti). The same exposure time and gains were used for each channel across all samples. For P30 mice, images were analyzed in a threshold-independent way. First, background fluorescence values were calculated from non-LGN regions and used to be subtracted from images. Then, images were normalized by adjusting the contrast to 5% saturation. For each pixel, R-value was computed as  $R = \log_{10}(F_{\text{ipsi}}/F_{\text{contra}})$ , where  $F_{\text{ipsi}}$  or  $F_{\text{contra}}$  is the fluorescence intensity of the pixel in ipsilateral or contralateral channel, respectively. Those pixels whose values equal to zero were excluded. Over 99.5% of R-values ranged between -3 and 2, and they were plotted as a distribution graph. The variance of R-values was computed to quantify the extent of segregation. The greater variance means more segregation between ipsilateral and



contralateral RGC inputs. The full code can be found here: [https://github.com/TaoLi322/Microglia\\_GPR56\\_Synapse/blob/master/Eye-Seg\\_R-value](https://github.com/TaoLi322/Microglia_GPR56_Synapse/blob/master/Eye-Seg_R-value).

For P10 mice, 1  $\mu$ l of 0.2% CTB488 and CTB594 (Life Technologies, C22842) was injected into the left or right eye, respectively. The percentage of overlapped left and right eye projections in dLGN was quantified using a multi-threshold quantitative method, as described before (Torborg & Feller, 2004).

### LGN slice preparation and electrophysiology

Mice (P28–P34) were decapitated; their brains were removed and placed in a 4°C choline solution, containing 78.3 mM NaCl, 23 mM NaHCO<sub>3</sub>, 23 mM glucose, 33.8 mM choline chloride, 2.3 mM KCl, 1.1 mM NaH<sub>2</sub>PO<sub>3</sub>, 6.4 mM MgCl<sub>2</sub>, and 0.45 mM CaCl<sub>2</sub>. The two hemispheres were then separated by an angled cut (3°–5°) relative to the cerebral longitudinal fissure. The medial aspect of the right hemisphere was then glued onto an angled (20°) agar block, and 250  $\mu$ m LGN slices were cut in ice-cold, choline solutions using a vibratome (Leica VT1200S) based upon previously described protocols (Turner & Salt, 1998; Chen & Regehr, 2000). Slices were allowed to recover at 33°C for 30 min in choline solution and then for an additional 30–50 min in artificial cerebral spinal fluid (ACSF). ACSF contained 125 mM NaCl, 25 mM NaHCO<sub>3</sub>, 25 mM glucose, 2.5 mM KCl, 1.25 mM NaH<sub>2</sub>PO<sub>3</sub>, 1 mM MgCl<sub>2</sub>, and 2 mM CaCl<sub>2</sub>. All solutions were continuously supplied with oxygen (95% O<sub>2</sub>/5% CO<sub>2</sub>).

Whole-cell voltage-clamp recordings of neurons from the dLGN were conducted using a MultiClamp 700B amplifier, digitized with a Digidata 1440A, collected with Clampex 10.2, and analyzed using Clampfit 10.2 (Axon Instruments). The slice containing dLGN was perfused with oxygenated ACSF, supplemented with 50  $\mu$ M picrotoxin. Neurons were then patched using glass electrodes (3–4 M $\Omega$ ) filled with 35 mM CsF, 100 mM CsCl, 10 mM EGTA, 10 mM HEPES, and 0.1 mM D600 (methoxyverapamil hydrochloride). Internal solution has a pH of 7.32 with CsOH. ACSF filled glass pipettes were placed in the optic tract, and these stimulating electrodes were moved repeatedly until reaching the location that gave the largest postsynaptic response. The maximum AMPA and NMDA currents were then determined by gradually increasing the stimulus intensity from 0.1 up to 1 mA. The maximum response size was considered to be the amplitude of the response after three consecutive increases in stimulation intensity failed to result in a larger response, or if the response amplitude decreased with an increase in stimulation intensity. AMPA responses were collected at –70 mV and NMDA responses at +40 mV, and were collected with alternate stimulations. To confirm that the optic tracts and not cortical inputs were stimulated, paired pulse data with a 50 ms interstimulus interval were collected, given that optic inputs usually demonstrate paired pulse depression, and cortical inputs paired pulse facilitation. No difference in paired pulse depression was seen between control and conditional knockout mice (Appendix Fig S9,  $P = 0.694$ , Student's *t*-test).

### Statistical analysis

For all quantification, images were acquired blindly to genotype before quantification. All data are shown as mean  $\pm$  SD or

mean  $\pm$  SEM as indicated in figure legends. Asterisks indicate significance: \*\*\*\* $P < 0.0001$ , \*\*\* $P < 0.001$ , \*\* $P < 0.01$ , \* $P < 0.05$ . All effects of genotype were analyzed by Student's *t*-test, one-way ANOVA, or two-way ANOVA (Graph Pad Software, Inc).

## Data availability

This study includes no data deposited in external repositories.

**Expanded View** for this article is available online.

### Acknowledgments

We thank Dr. Chinfai Chen at Boston Children's Hospital for technical support on electrophysiology and thoughtful discussion on the manuscript, Douglas Richardson at Harvard Imaging Core for kind technical support on SIM imaging, Alexandre Tiriach and Marla Feller for kindly providing technical support on eye segregation analysis, Aashish Manglik for the Alexa Fluor 647 NHS Ester labeling kit and technical support, Dr. Scott Manalis for the Ba/F3 cell line, Dr. Greg Lemke at Salk Institute for sharing GAS6 plasmids and Dario Tejera, Eric Huang, Anna Molofsky, Mercedes Paredes, and Kelly Monk for critical reading of the manuscript. This research was supported in part by NINDS grants R01 NS094164 (X.P.), R21NS108312 (X.P.), R01NS108446 (X.P.), and a sponsored research agreement with Biogen (X.P.).

### Author contributions

TL and XP conceived and designed the experiments, performed data analyses, and wrote the manuscript. TL Performed most experiments. BC CKG, TK, SG, RL, DY and HCO contributed to experiments and data analysis. EJ-V and HU designed, performed, and analyzed the electrophysiology experiments. AKM and BS assisted on synapse quantification and *in vivo* engulfment assay. All authors read and edited the manuscript.

### Conflict of interest

The authors declare that they have no conflict of interest.

## References

- Ackerman SD, Garcia C, Piao X, Gutmann DH, Monk KR (2015) The adhesion GPCR Gpr56 regulates oligodendrocyte development via interactions with G $\alpha$  12/13 and RhoA. *Nat Commun* 6: 6122
- Araç D, Boucard AA, Bolliger MF, Nguyen J, Soltis SM, Sudhof TC, Brunger AT (2012) A novel evolutionarily conserved domain of cell-adhesion GPCRs mediates autoproteolysis. *EMBO J* 31: 1364–1378
- Bennett ML, Bennett FC, Liddelow SA, Ajami B, Zamanian JL, Fernhoff NB, Mulinyawe SB, Bohlen CJ, Adil A, Tucker A et al (2016) New tools for studying microglia in the mouse and human CNS. *Proc Natl Acad Sci USA* 113: E1738–E1746
- Bennett FC, Bennett ML, Yaqoob F, Mulinyawe SB, Grant GA, Hayden Gephart M, Plowey ED, Barres BA (2018) A combination of ontogeny and cns environment establishes microglial identity. *Neuron* 98: 1170–1183.e1178
- Beyers EM, Williamson PL (2016) Getting to the outer leaflet: physiology of phosphatidylserine exposure at the plasma membrane. *Physiol Rev* 96: 605–645
- Bialas AR, Presumey J, Das A, van der Poel CE, Lapchak PH, Mesin L, Victoria G, Tsokos GC, Mawrin C, Herbst R et al (2017) Microglia-

- dependent synapse loss in type I interferon-mediated lupus. *Nature* 546: 539–543
- Bohlen CJ, Bennett FC, Tucker AF, Collins HY, Mulinyawe SB, Barres BA (2017) Diverse requirements for microglial survival, specification, and function revealed by defined-medium cultures. *Neuron* 94: 759–773.e758
- Braunschweig U, Gueroussov S, Plocik AM, Graveley BR, Blencowe BJ (2013) Dynamic integration of splicing within gene regulatory pathways. *Cell* 152: 1252–1269
- Cermak N, Olcum S, Delgado FF, Wasserman SC, Payer KR, A Murakam M, Knudsen SM, Kimmerling RJ, Stevens MM, Kikuchi Y et al (2016) High-throughput measurement of single-cell growth rates using serial microfluidic mass sensor arrays. *Nat Biotechnol* 34: 1052–1059
- Chen C, Regehr WG (2000) Developmental remodeling of the retinogeniculate synapse. *Neuron* 28: 955–966
- Chu VT, Weber T, Graf R, Sommermann T, Petsch K, Sack U, Volchkov P, Rajewsky K, Kuhn R (2016) Efficient generation of Rosa26 knock-in mice using CRISPR/Cas9 in C57BL/6 zygotes. *BMC Biotechnol* 16: 4
- Chung WS, Clarke LE, Wang GX, Stafford BK, Sher A, Chakraborty C, Joung J, Foo LC, Thompson A, Chen C et al (2013) Astrocytes mediate synapse elimination through MEGF10 and MERTK pathways. *Nature* 504: 394–400
- Cronk JC, Filiano AJ, Louveau A, Marin I, Marsh R, Ji E, Goldman DH, Smirnov I, Geraci N, Acton S et al (2018) Peripherally derived macrophages can engraft the brain independent of irradiation and maintain an identity distinct from microglia. *J Exp Med* 215: 1627–1647
- Dani A, Huang B, Bergan J, Dulac C, Zhuang X (2010) Superresolution imaging of chemical synapses in the brain. *Neuron* 68: 843–856
- Djurisic M, Brott BK, Saw NL, Shamloo M, Shatz CJ (2019) Activity-dependent modulation of hippocampal synaptic plasticity via PirB and endocannabinoids. *Mol Psychiatry* 24: 1206–1219
- Erturk A, Wang Y, Sheng M (2014) Local pruning of dendrites and spines by caspase-3-dependent and proteasome-limited mechanisms. *J Neurosci* 34: 1672–1688
- Exteberria A, Hokanson KC, Dao DQ, Mayoral SR, Mei F, Redmond SA, Ullian EM, Chan JR (2016) Dynamic modulation of myelination in response to visual stimuli alters optic nerve conduction velocity. *J Neurosci* 36: 6937–6948
- Feng W, Yasumura D, Matthes MT, LaVail MM, Vollrath D (2002) Mertk triggers uptake of photoreceptor outer segments during phagocytosis by cultured retinal pigment epithelial cells. *J Biol Chem* 277: 17016–17022
- Fitzpatrick D, Usrey WM, Schofield BR, Einstein G (1994) The sublaminar organization of corticogeniculate neurons in layer 6 of macaque striate cortex. *Vis Neurosci* 11: 307–315
- Folts CJ, Giera S, Li T, Piao X (2019) Adhesion G protein-coupled receptors as drug targets for neurological diseases. *Trends Pharmacol Sci* 40: 278–293
- Frank MG, Wieseler-Frank JL, Watkins LR, Maier SF (2006) Rapid isolation of highly enriched and quiescent microglia from adult rat hippocampus: immunophenotypic and functional characteristics. *J Neurosci Methods* 151: 121–130
- Fujiyama F, Hioki H, Tomioka R, Taki K, Tamamaki N, Nomura S, Okamoto K, Kaneko T (2003) Changes of immunocytochemical localization of vesicular glutamate transporters in the rat visual system after the retinofugal denervation. *J Comp Neurol* 465: 234–249
- Fujiyama F, Kuramoto E, Okamoto K, Hioki H, Furuta T, Zhou L, Nomura S, Kaneko T (2004) Presynaptic localization of an AMPA-type glutamate receptor in corticostriatal and thalamostriatal axon terminals. *Eur J Neurosci* 20: 3322–3330
- Giera S, Deng Y, Luo R, Ackerman SD, Mogha A, Monk KR, Ying Y, Jeong SJ, Makinodan M, Bialas AR et al (2015) The adhesion G protein-coupled receptor GPR56 is a cell-autonomous regulator of oligodendrocyte development. *Nat Commun* 6: 6121
- Giera S, Luo R, Ying Y, Ackerman SD, Jeong SJ, Stoveken HM, Folts CJ, Welsh CA, Tall GG, Stevens B et al (2018) Microglial transglutaminase-2 drives myelination and myelin repair via GPR56/ADGRG1 in oligodendrocyte precursor cells. *Elife* 7: e33385
- Gosselin D, Link VM, Romanoski CE, Fonseca GJ, Eichenfield DZ, Spann NJ, Stender JD, Chun HB, Garner H, Geissmann F et al (2014) Environment drives selection and function of enhancers controlling tissue-specific macrophage identities. *Cell* 159: 1327–1340
- Gosselin D, Skola D, Coufal NG, Holtman IR, Schlachetzki JCM, Sajti E, Jaeger BN, O'Connor C, Fitzpatrick C, Pasillas MP et al (2017) An environment-dependent transcriptional network specifies human microglia identity. *Science* 356: eaal3222
- Györfy BA, Kun J, Torok G, Bulyaki E, Borhegyi Z, Gulyassy P, Kis V, Szocsics P, Micsonai A, Matko J et al (2018) Local apoptotic-like mechanisms underlie complement-mediated synaptic pruning. *Proc Natl Acad Sci USA* 115: 6303–6308
- Hagemeyer N, Hanft KM, Akritidou MA, Unger N, Park ES, Stanley ER, Staszewski O, Dimou L, Prinz M (2017) Microglia contribute to normal myelinogenesis and to oligodendrocyte progenitor maintenance during adulthood. *Acta Neuropathol* 134: 441–458
- Hamann J, Aust G, Arac D, Engel FB, Formstone C, Fredriksson R, Hall RA, Harty BL, Kirchhoff C, Knapp B et al (2015) International union of basic and clinical pharmacology. XCIV. Adhesion G protein-coupled receptors. *Pharmacol Rev* 67: 338–367
- Hanshaw RG, Smith BD (2005) New reagents for phosphatidylserine recognition and detection of apoptosis. *Bioorg Med Chem* 13: 5035–5042
- Hong S, Beja-Glasser VF, Nfonoyim BM, Frouin A, Li S, Ramakrishnan S, Merry KM, Shi Q, Rosenthal A, Barres BA et al (2016) Complement and microglia mediate early synapse loss in Alzheimer mouse models. *Science* 352: 712–716
- Hong S, Wilton DK, Stevens B, Richardson DS (2017) Structured illumination microscopy for the investigation of synaptic structure and function. *Methods Mol Biol* 1538: 155–167
- Ingolfsson HI, Melo MN, van Eerden FJ, Arnarez C, Lopez CA, Wassenaar TA, Periole X, de Vries AH, Tieleman DP, Marrink SJ (2014) Lipid organization of the plasma membrane. *J Am Chem Soc* 136: 14554–14559
- Jeong SJ, Li S, Luo R, Strokes N, Piao X (2012a) Loss of Col3a1, the gene for Ehlers-Danlos syndrome type IV, results in neocortical dyslamination. *PLoS One* 7: e29767
- Jeong SJ, Luo R, Li S, Strokes N, Piao X (2012b) Characterization of G protein-coupled receptor 56 protein expression in the mouse developing neocortex. *J Comp Neurol* 520: 2930–2940
- Kim JE, Han JM, Park CR, Shin KJ, Ahn C, Seong JY, Hwang JI (2010) Splicing variants of the orphan G-protein-coupled receptor GPR56 regulate the activity of transcription factors associated with tumorigenesis. *J Cancer Res Clin Oncol* 136: 47–53
- Koopman G, Reutelingsperger CP, Kuijten GA, Keehnen RM, Pals ST, van Oers MH (1994) Annexin V for flow cytometric detection of phosphatidylserine expression on B cells undergoing apoptosis. *Blood* 84: 1415–1420
- Koulov AV, Stucker KA, Lakshmi C, Robinson JP, Smith BD (2003) Detection of apoptotic cells using a synthetic fluorescent sensor for membrane surfaces that contain phosphatidylserine. *Cell Death Differ* 10: 1357–1359

- Land PW, Kyonka E, Shamalla-Hannah L (2004) Vesicular glutamate transporters in the lateral geniculate nucleus: expression of VGLUT2 by retinal terminals. *Brain Res* 996: 251–254
- Langenhan T, Piao X, Monk KR (2016) Adhesion G protein-coupled receptors in nervous system development and disease. *Nat Rev Neurosci* 17: 550–561
- Lee H, Brott BK, Kirkby LA, Adelson JD, Cheng S, Feller MB, Datwani A, Shatz CJ (2014) Synapse elimination and learning rules co-regulated by MHC class I H2-Db. *Nature* 509: 195–200
- Lehrman EK, Wilton DK, Litvina EY, Welsh CA, Chang ST, Frouin A, Walker AJ, Heller MD, Umemori H, Chen C et al (2018) CD47 protects synapses from excess microglia-mediated pruning during development. *Neuron* 100: 120–134.e126
- Lemke G (2013) Biology of the TAM receptors. *Cold Spring Harb Perspect Biol* 5: a009076
- Li S, Jin Z, Koirala S, Bu L, Xu L, Hynes RO, Walsh CA, Corfas G, Piao X (2008) GPR56 regulates pial basement membrane integrity and cortical lamination. *J Neurosci* 28: 5817–5826
- Luo R, Jeong SJ, Jin Z, Strokes N, Li S, Piao X (2011) G protein-coupled receptor 56 and collagen III, a receptor-ligand pair, regulates cortical development and lamination. *Proc Natl Acad Sci USA* 108: 12925–12930
- Luo R, Jin Z, Deng Y, Strokes N, Piao X (2012) Disease-associated mutations prevent GPR56-collagen III interaction. *PLoS One* 7: e29818
- Mark MR, Chen J, Hammonds RG, Sadick M, Godowski PJ (1996) Characterization of Gas6, a member of the superfamily of G domain-containing proteins, as a ligand for Rse and Axl. *J Biol Chem* 271: 9785–9789
- Matcovitch-Natan O, Winter DR, Giladi A, Vargas Aguilar S, Spinrad A, Sarrazin S, Ben-Yehuda H, David E, Zelada Gonzalez F, Perrin P et al (2016) Microglia development follows a stepwise program to regulate brain homeostasis. *Science* 353: aad8670
- Mattson MP, Keller JN, Begley JG (1998) Evidence for synaptic apoptosis. *Exp Neurol* 153: 35–48
- Mayoral SR, Etxeberria A, Shen YA, Chan JR (2018) Initiation of CNS myelination in the optic nerve is dependent on axon caliber. *Cell Rep* 25: 544–550.e543
- Mazaheri F, Breus O, Durdu S, Haas P, Wittbrodt J, Gilmour D, Peri F (2014) Distinct roles for BAI1 and TIM-4 in the engulfment of dying neurons by microglia. *Nat Commun* 5: 4046
- McLaughlin S, Murray D (2005) Plasma membrane phosphoinositide organization by protein electrostatics. *Nature* 438: 605–611
- Miyamoto A, Wake H, Ishikawa AW, Eto K, Shibata K, Murakoshi H, Koizumi S, Moorhouse AJ, Yoshimura Y, Nabekura J (2016) Microglia contact induces synapse formation in developing somatosensory cortex. *Nat Commun* 7: 12540
- Miyanishi M, Tada K, Koike M, Uchiyama Y, Kitamura T, Nagata S (2007) Identification of Tim4 as a phosphatidylserine receptor. *Nature* 450: 435–439
- Nadal-Nicolas FM, Jimenez-Lopez M, Sobrado-Calvo P, Nieto-Lopez L, Canovas-Martinez I, Salinas-Navarro M, Vidal-Sanz M, Agudo M (2009) Brn3a as a marker of retinal ganglion cells: qualitative and quantitative time course studies in naive and optic nerve-injured retinas. *Invest Ophthalmol Vis Sci* 50: 3860–3868
- Nagata K, Ohashi K, Nakano T, Arita H, Zong C, Hanafusa H, Mizuno K (1996) Identification of the product of growth arrest-specific gene 6 as a common ligand for Axl, Sky, and Mer receptor tyrosine kinases. *J Biol Chem* 271: 30022–30027
- Nagata S, Suzuki J, Segawa K, Fujii T (2016) Exposure of phosphatidylserine on the cell surface. *Cell Death Differ* 23: 952–961
- Neher JJ, Emmrich JV, Fricker M, Mander PK, They C, Brown GC (2013) Phagocytosis executes delayed neuronal death after focal brain ischemia. *Proc Natl Acad Sci USA* 110: E4098–E4107
- Ohashi K, Nagata K, Toshima J, Nakano T, Arita H, Tsuda H, Suzuki K, Mizuno K (1995) Stimulation of sky receptor tyrosine kinase by the product of growth arrest-specific gene 6. *J Biol Chem* 270: 22681–22684
- Paolicelli RC, Bolasco G, Pagani F, Maggi L, Scianni M, Panzanelli P, Giustetto M, Ferreira TA, Guiducci E, Dumas L et al (2011) Synaptic pruning by microglia is necessary for normal brain development. *Science* 333: 1456–1458
- Paradies G, Paradies V, De Benedictis V, Ruggiero FM, Petrosillo G (2014) Functional role of cardiolipin in mitochondrial bioenergetics. *Biochim Biophys Acta* 1837: 408–417
- Park D, Tosello-Trampont AC, Elliott MR, Lu M, Haney LB, Ma Z, Klibanov AL, Mandell JW, Ravichandran KS (2007) BAI1 is an engulfment receptor for apoptotic cells upstream of the ELMO/Dock180/Rac module. *Nature* 450: 430–434
- Park SY, Jung MY, Kim HJ, Lee SJ, Kim SY, Lee BH, Kwon TH, Park RW, Kim IS (2008) Rapid cell corpse clearance by stabilin-2, a membrane phosphatidylserine receptor. *Cell Death Differ* 15: 192–201
- Parkhurst CN, Yang G, Ninan I, Savas JN, Yates JR III, Lafaille JJ, Hempstead BL, Littman DR, Gan WB (2013) Microglia promote learning-dependent synapse formation through brain-derived neurotrophic factor. *Cell* 155: 1596–1609
- Piao X, Hill RS, Bodell A, Chang BS, Basel-Vanagaite L, Straussberg R, Dobyns WB, Qasrawi B, Winter RM, Innes AM et al (2004) G protein-coupled receptor-dependent development of human frontal cortex. *Science* 303: 2033–2036
- Piao X, Chang BS, Bodell A, Woods K, Benzeev B, Topcu M, Guerrini R, Goldberg-Stern H, Sztrihai L, Dobyns WB et al (2005) Genotype-phenotype analysis of human frontoparietal polymicrogyria syndromes. *Ann Neurol* 58: 680–687
- Reemst K, Noctor SC, Lucassen PJ, Hol EM (2016) The indispensable roles of microglia and astrocytes during brain development. *Front Hum Neurosci* 10: 566
- Salzman GS, Ackerman SD, Ding C, Koide A, Leon K, Luo R, Stoveken HM, Fernandez CG, Tall GG, Piao X et al (2016) Structural basis for regulation of GPR56/ADGRG1 by its alternatively spliced extracellular domains. *Neuron* 91: 1292–1304
- Sato K (2015) Effects of microglia on neurogenesis. *Glia* 63: 1394–1405
- Schafer DP, Lehrman EK, Kautzman AG, Koyama R, Mardinly AR, Yamasaki R, Ransohoff RM, Greenberg ME, Barres BA, Stevens B (2012) Microglia sculpt postnatal neural circuits in an activity and complement-dependent manner. *Neuron* 74: 691–705
- Schwenk F, Baron U, Rajewsky K (1995) A cre-transgenic mouse strain for the ubiquitous deletion of loxP-flanked gene segments including deletion in germ cells. *Nucleic Acids Res* 23: 5080–5081
- Segawa K, Suzuki J, Nagata S (2011) Constitutive exposure of phosphatidylserine on viable cells. *Proc Natl Acad Sci USA* 108: 19246–19251
- Segawa K, Nagata S (2015) An apoptotic ‘Eat Me’ Signal: phosphatidylserine exposure. *Trends Cell Biol* 25: 639–650
- Sekar A, Bialas AR, de Rivera H, Davis A, Hammond TR, Kamitaki N, Tooley K, Presumey J, Baum M, Van Doren V et al (2016) Schizophrenia risk from complex variation of complement component 4. *Nature* 530: 177–183
- Sellgren CM, Gracias J, Watmuff B, Biag JD, Thanos JM, Whittredge PB, Fu T, Worringer K, Brown HE, Wang J et al (2019) Increased synapse elimination by microglia in schizophrenia patient-derived models of synaptic pruning. *Nat Neurosci* 22: 374–385

- Shatz CJ, Kirkwood PA (1984) Prenatal development of functional connections in the cat's retinogeniculate pathway. *J Neurosci* 4: 1378–1397
- Sherman SM, Guillery RW (1996) Functional organization of thalamocortical relays. *J Neurophysiol* 76: 1367–1395
- Sherman SM, Guillery RW (1998) On the actions that one nerve cell can have on another: distinguishing “drivers” from “modulators”. *Proc Natl Acad Sci USA* 95: 7121–7126
- Singer K, Luo R, Jeong SJ, Piao X (2013) GPR56 and the developing cerebral cortex: cells, matrix, and neuronal migration. *Mol Neurobiol* 47: 186–196
- Smith BA, Gammon ST, Xiao S, Wang W, Chapman S, McDermott R, Suckow MA, Johnson JR, Piwnicka-Worms D, Gokel GW et al (2011) *In vivo* optical imaging of acute cell death using a near-infrared fluorescent zinc-dipicolylamine probe. *Mol Pharm* 8: 583–590
- Sretavan D, Shatz CJ (1984) Prenatal development of individual retinogeniculate axons during the period of segregation. *Nature* 308: 845–848
- Stevens B, Allen NJ, Vazquez LE, Howell GR, Christopherson KS, Nouri N, Micheva KD, Mehalow AK, Huberman AD, Stafford B et al (2007) The classical complement cascade mediates CNS synapse elimination. *Cell* 131: 1164–1178
- Stitt TN, Conn G, Gore M, Lai C, Bruno J, Radziejewski C, Mattsson K, Fisher J, Gies DR, Jones PF et al (1995) The anticoagulation factor protein S and its relative, Gas6, are ligands for the Tyro 3/Axl family of receptor tyrosine kinases. *Cell* 80: 661–670
- Suh J, Rivest AJ, Nakashiba T, Tominaga T, Tonegawa S (2011) Entorhinal cortex layer III input to the hippocampus is crucial for temporal association memory. *Science* 334: 1415–1420
- Suzuki J, Umeda M, Sims PJ, Nagata S (2010) Calcium-dependent phospholipid scrambling by TMEM16F. *Nature* 468: 834–838
- Swanson LW, Wyss JM, Cowan WM (1978) An autoradiographic study of the organization of intrahippocampal association pathways in the rat. *J Comp Neurol* 181: 681–715
- Tang G, Gudsnek K, Kuo SH, Cotrina ML, Rosoklija G, Sosunov A, Sonders MS, Kanter E, Castagna C, Yamamoto A et al (2014) Loss of mTOR-dependent macroautophagy causes autistic-like synaptic pruning deficits. *Neuron* 83: 1131–1143
- Thomson AM (2010) Neocortical layer 6, a review. *Front Neuroanat* 4: 13
- Tiriac A, Smith BE, Feller MB (2018) Light prior to eye opening promotes retinal waves and eye-specific segregation. *Neuron* 100: 1059–1065.e1054
- Torborg CL, Feller MB (2004) Unbiased analysis of bulk axonal segregation patterns. *J Neurosci Methods* 135: 17–26
- Tufail Y, Cook D, Fourgeaud L, Powers CJ, Merten K, Clark CL, Hoffman E, Ngo A, Sekiguchi KJ, O'Shea CC et al (2017) Phosphatidylserine exposure controls viral innate immune responses by microglia. *Neuron* 93: 574–586.e578
- Turner JP, Salt TE (1998) Characterization of sensory and corticothalamic excitatory inputs to rat thalamocortical neurones *in vitro*. *J Physiol* 510(Pt 3): 829–843
- Vainchtein ID, Chin G, Cho FS, Kelley KW, Miller JG, Chien EC, Liddel SA, Nguyen PT, Nakao-Inoue H, Dorman LC et al (2018) Astrocyte-derived interleukin-33 promotes microglial synapse engulfment and neural circuit development. *Science* 359: 1269–1273
- Vasek MJ, Garber C, Dorsey D, Durrant DM, Bollman B, Soung A, Yu J, Perez-Torres C, Frouin A, Wilton DK et al (2016) A complement-microglial axis drives synapse loss during virus-induced memory impairment. *Nature* 534: 538–543
- Yang L, Chen G, Mohanty S, Scott G, Fazal F, Rahman A, Begum S, Hynes RO, Xu L (2011) GPR56 Regulates VEGF production and angiogenesis during melanoma progression. *Cancer Res* 71: 5558–5568
- Yona S, Kim KW, Wolf Y, Mildner A, Varol D, Breker M, Strauss-Ayali D, Viukov S, Guillemins M, Misharin A et al (2013) Fate mapping reveals origins and dynamics of monocytes and tissue macrophages under homeostasis. *Immunity* 38: 79–91
- Zachowski A, Henry JP, Devaux PF (1989) Control of transmembrane lipid asymmetry in chromaffin granules by an ATP-dependent protein. *Nature* 340: 75–76
- Zhang Y, Chen K, Sloan SA, Bennett ML, Scholze AR, O'Keefe S, Phatnani HP, Guarnieri P, Caneda C, Ruderisch N et al (2014) An RNA-sequencing transcriptome and splicing database of glia, neurons, and vascular cells of the cerebral cortex. *J Neurosci* 34: 11929–11947